# Hybrid Metal-Ligand Interfacial Dipole Engineering of Functional Plasmonic Nanostructures for Extraordinary Responses of Optoelectronic Properties

Sumon Hati,[1] Xuehui Yang,[2] Prashant Gupta,[3] Barry B. Muhoberac,[1] Jingzhi Pu,[1] Jing Zhang,[2] and Rajesh Sardar[1,*]

Department of Chemistry and Chemical Biology, Indiana University-Purdue University Indianapolis, Indianapolis, Indiana 46202, United States

Department of Mechanical and Energy engineering, Indiana University-Purdue University Indianapolis, Indianapolis, Indiana 46202, United States

Department of Mechanical Engineering, Washington University, St. Louis, Missouri 63130, United States

*Corresponding Author's email: rsardar@iupui.edu (R.S)

## Abstract:

Programmable manipulation of inorganic-organic interfacial electronic properties of ligand-functionalized plasmonic nanoparticles (NPs) is the key parameter dictating their applications such as catalysis, photovoltaics, and biosensing. Here we report the localized surface plasmon resonance (LSPR) properties of gold triangular nanoprisms (Au TNPs) in solid-state that are functionalized with dipolar, conjugated ligands. A library of thiocinnamate ligands with varying surface dipole moments were used to functionalize TNPs, which results in ~150 nm reversible tunability of LSPR peak wavelength with significant peak broadening (~230 meV). The highly adjustable chemical system of thiocinnamate ligands is capable of shifting the Au work function down to 2.4 eV versus vacuum, i.e., ~2.9 eV lower than a clean Au (111) surface, and this work function can be modulated up to 3.3 eV, the largest value reported to date through the formation of organothiolate SAMs on Au. Interestingly, the magnitude of plasmonic responses and work function modulation is NP shape dependent. By combining first principle calculations and experiments, we have established the mechanism of direct wavefunction delocalization of electrons residing near the Fermi level into hybrid electronic states that are mostly dictated by the inorganic-organic interfacial dipole moments. We determine that both interfacial dipole and hybrid electronic states, and vinyl conjugation together are the key to achieving such extraordinary changes in the optoelectronic properties of ligand-functionalized, plasmonic NPs. The present study provides a quantitative relationship describing how specifically constructed organic ligands can be used to control the interfacial properties of NPs and thus the plasmonic and electronic responses of these functional plasmonics for a wide range of plasmon-driven applications.

**Keywords:** gold nanoparticles, localized surface plasmon resonance, dipole moment, surface passivating ligand, inorganic-organic interface, work function

### Table of Content (TOC)

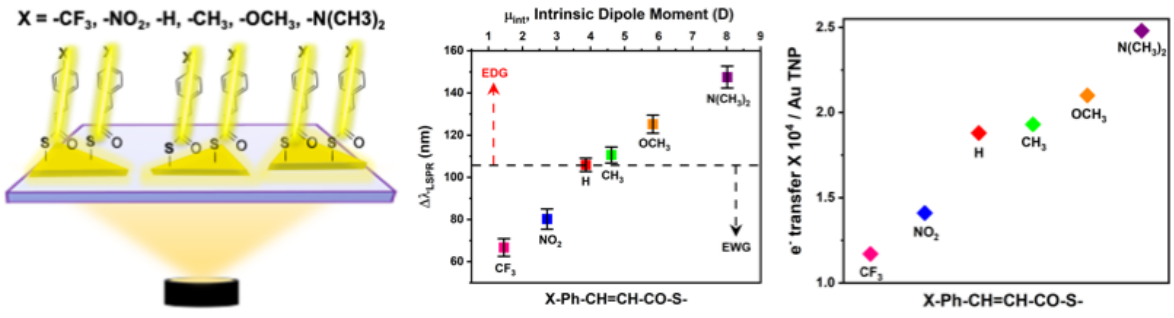

Surface ligand chemistry is ubiquitously associated with colloidally synthesized nanoparticles (NPs) to preserve and enhance their plasmonic properties over a wide range of applications.[1-11] Functionalization of noble metal (Ag and Au) NPs with organic surface ligands forming a self-assembled monolayer (SAM) alters the local dielectric environment that results in modulation of NP localized surface plasmon resonance (LSPR) properties originating from the collective oscillation of free conduction band electrons upon light exposure.[1] LSPR active NPs have been extensively studied for biosensing applications,[2, 3] and various energy conversion schemes.[4-6] In this context, the metal-ligand chemical interaction can influence the plasmonic properties such as broadening, intensity change and shifting of the LSPR peak in the ligand-functionalized NPs.[12] Two factors significantly contribute to the LSPR spectra changes: (1) chemical interface damping (CID) where a direct electron transfer occurs at the metal-ligand interfacial orbitals i.e., hybrid orbitals that contain properties of both inorganic metal and organic passivating ligands, and (2) delocalization of electron wave functions in metal-ligand interfacial orbitals.[13] Both mechanisms change the electron density of metal thus altering the LSPR properties. Therefore, it is not just the structure of the NP core but also the ligand chemistry that dictates the performance of ligand-passivated plasmonic NPs for specific plasmonic-based applications.

The ligand-controlled tuning of NP LSPR properties has been explored for a long time, yet most ligand choices showed very limited plasmonic responses, in their LSPR peak shift and broadening. Few reports have described the organic ligand effects influencing the plasmonic properties of Au NPs, either because of the CID[14-16] or reversible transfer of electron density between the NP and ligand leading to a change in the NP free electron density.[13] In the event of interfacial electron transfer or delocalization, one would expect that the energetic states of hybrid orbitals that are formed from the interaction between the NP and ligands would dictate the extent of such electronic processes. Thus, it is the intrinsic ligand dipole that should, through ligand binding, control the metal-ligand interfacial (surface) dipole moment, which is expected to influence the Fermi level ($E_F$) of the ligand-functionalized metal NPs, their hybrid orbital energetic states, and density of states near the $E_F$. These changes will trigger the direct delocalization of electron wavefunctions from the $E_F$ to hybrid states, if energetically favourable. Therefore, the organic ligands varying intrinsic dipole moments will not only have the ability of participating in wavefunction delocalization mechanisms but also of controlling the overall LSPR responses. Together, appropriately selected surface ligands will allow very large shifts of the LSPR peak as well as broadening upon functionalization of noble metal NPs, which are yet to be studied to enable further improvement of the fundamental understanding of interfacial electronic structure and

properties of the ligand-passivated NPs, as well as the fabrication of next generation plasmon-related devices and catalysts.

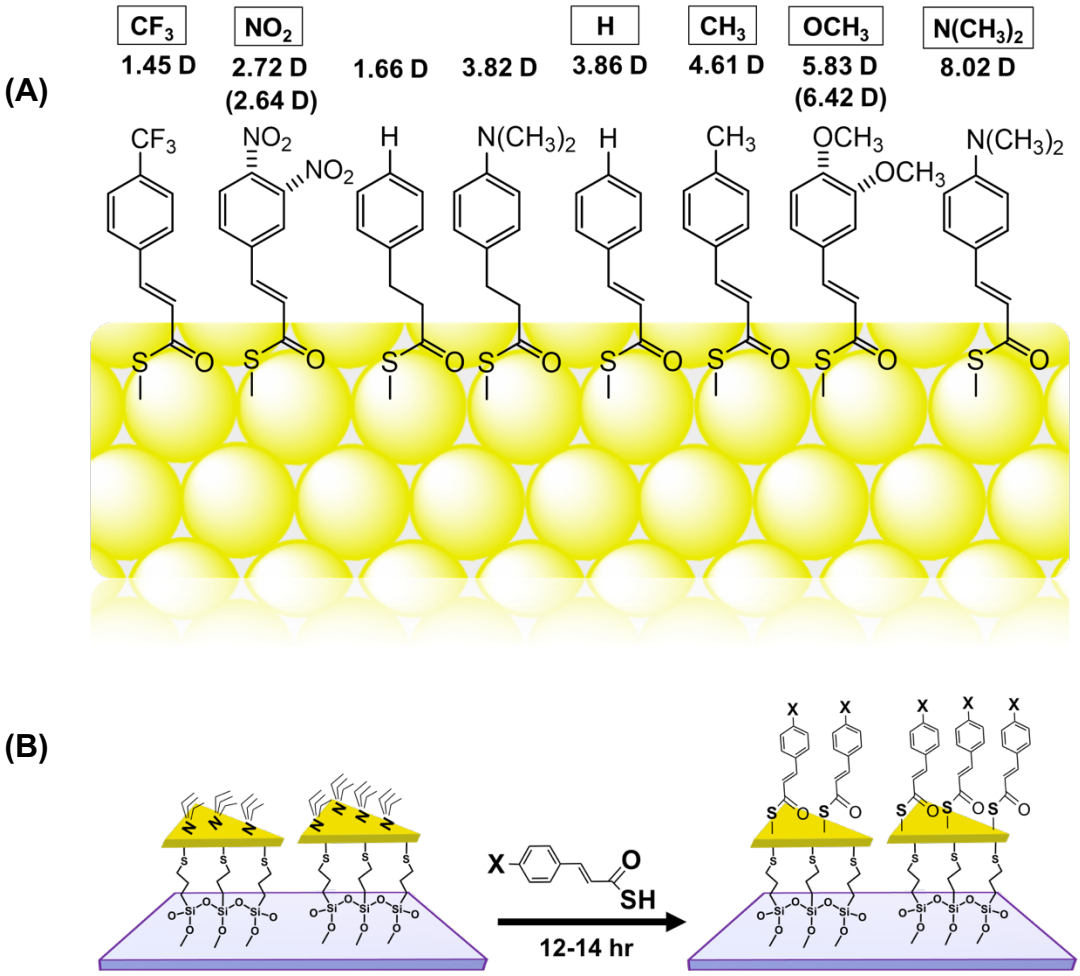


**Scheme 1. The model Au-TCA ligand system utilized in this study. (A)** Chemical structures and computed intrinsic dipole moments of free TCA ligands. Ligand attachment to Au (111) plane through a covalent Au-S bond are represented schematically. Yellow spheres indicate gold atoms rearranged in a Au TNPs most stabilized energy facet forming (111) plane. Notations in the box highlights the substituent groups in the aromatic ring of the TCA-X that were used to create our library of ligands. Dashed bonds indicate the position of the substituent in different stereo-structures of TCA variants. Dipole moments shown in parentheses indicate the intrinsic dipole moments for the meta substituents of TCA variants**. (B)** The surface modification approach in which weakly adsorbed triethylamine (TEA) ligands from the surface of Au TNPs are replaced with TCA-x ligands due to their strong Au-S interactions leading to SAM formation.

In this study, we report an extraordinarily large tuning of the LSPR dipole peak ($\lambda_{LSPR}$) position, line-width, and intensity of triethylamine (TEA)-passivated gold triangular nanoprisms (Au TNPs) upon functionalizing with a library of thiocinnamic ligands (TCA-X, -SCO-CH=CH-Ph-X, X = functional group) in the solid-state (**Scheme 1**). We consider our TCA-functionalized Au TNPs to be *functional plasmonics*. Depending on the electron withdrawing or donating character of the functional group (X), *i.e.,* by varying (1) the intrinsic dipole moments of ligands and (2) the interfacial dipole of the inorganic-organic interface, the

line-width, intensity, and the position ($\lambda_{LSPR}$) of the LSPR extinction peak of TNPs are dramatically, and importantly, reversibly altered. Ultraviolet photoelectron spectroscopy measurements were conducted to determine the work function of TCA-X-functionalized TNPs to further examine the effects of the dipole moment of ligands on the optoelectronic properties, and the work function of Au can be modulated up to 3.5 eV. Specifically, literature reports that the formation of aliphatic and/or aromatic hydrocarbon backbone containing-SAMs on Au can tune the work function 1.0-1.8 eV,[17-19] and thus we report here the largest change in work function to date for the thiolated SAM onto Au nanoparticle surface. Furthermore, SAMs from highly dipolar ligands are capable of lowering the work function of Au to 2.4 eV *versus vacuum*. Finally, utilizing first principle calculations, we investigated the interfacial metal-ligand bonding characteristics in light of the interfacial dipole moment, density of states (DOS), and hybrid orbital energies to examine our large changes in the plasmonic properties. We support our results based on calculations with the frontier orbital model of interfacial electronic states and find that the dimethylamine (X = -$N(CH_3)_2$) substitution in the TCA creates a highly energetically favourable lowest unoccupied molecular orbitals (LUMO), which could accept electronic charge as a form of delocalized electron wavefunction from the Fermi level ($E_F$) of ligand-passivated TNPs. Simplistically, -$N(CH_3)_2$ allows delocalization of electron wavefunctions into its aromatic ring even though it is an electron donating functional group. We expect that the control over LSPR response through manipulation of interfacial electronic properties of plasmonic noble metal-ligand hybrid systems will enhance their applications in nanoscale electronics and catalysis.

## Results and Discussion

**Surface functionalization and plasmonic properties of Au TNPs.** In order to study chemical effects on the surface plasmonic properties of Au TNPs from surface modification in metal-organic hybrid system, different para substituted TCAs varying electron donating (X = -$CH_3$, -$OCH_3$, -$N(CH_3)_2$) and electron withdrawing (X = -$CF_3$ and -$NO_2$) ability were covalently attached to Au TNPs and formed SAMs (**Scheme 1**). We chemically synthesized, and characterized all TCA ligands (See Supporting Information for Details and **Figure S1**). As shown in the scanning electron (SEM) and atomic force microscopy (AFM) images (**Figure 1A,B** and **Figure S2**), our chemically synthesized Au TNPs with ~42 nm edge length and ~9 nm in height were attached onto silanized glass. Then the surface of these triethylamine (TEA)-passivated TNPs was modified by HS-CO-CH=CH-Ph-X (TCA-X) ligands through ligand exchange in the solid-state. From herein, we classify each TCA ligand by its functional group (X). We have selected Au TNPs to study the ligand effects on the interfacial dipoles and resulting optoelectronic properties because: (1) Their sharp tips

produce strong EM-field enhancement, thus any small changes to physicochemical properties of the SAM composition will dramatically affect the properties (**Figure 1C**); (2) High electron density at the tips effectively create dipole pointing from interior to tips of TNPs[20-22] resulting in a large dipole influence at the metal-ligand interface controlled by the TCA-X SAM composition; (3) Strong soft-soft Au-S covalent interactions provide additional stability to SAMs for extensive spectroscopy and microscopy characterizations; (4) Flat TNP surfaces should allow the formation of tight SAMs of TCAs.

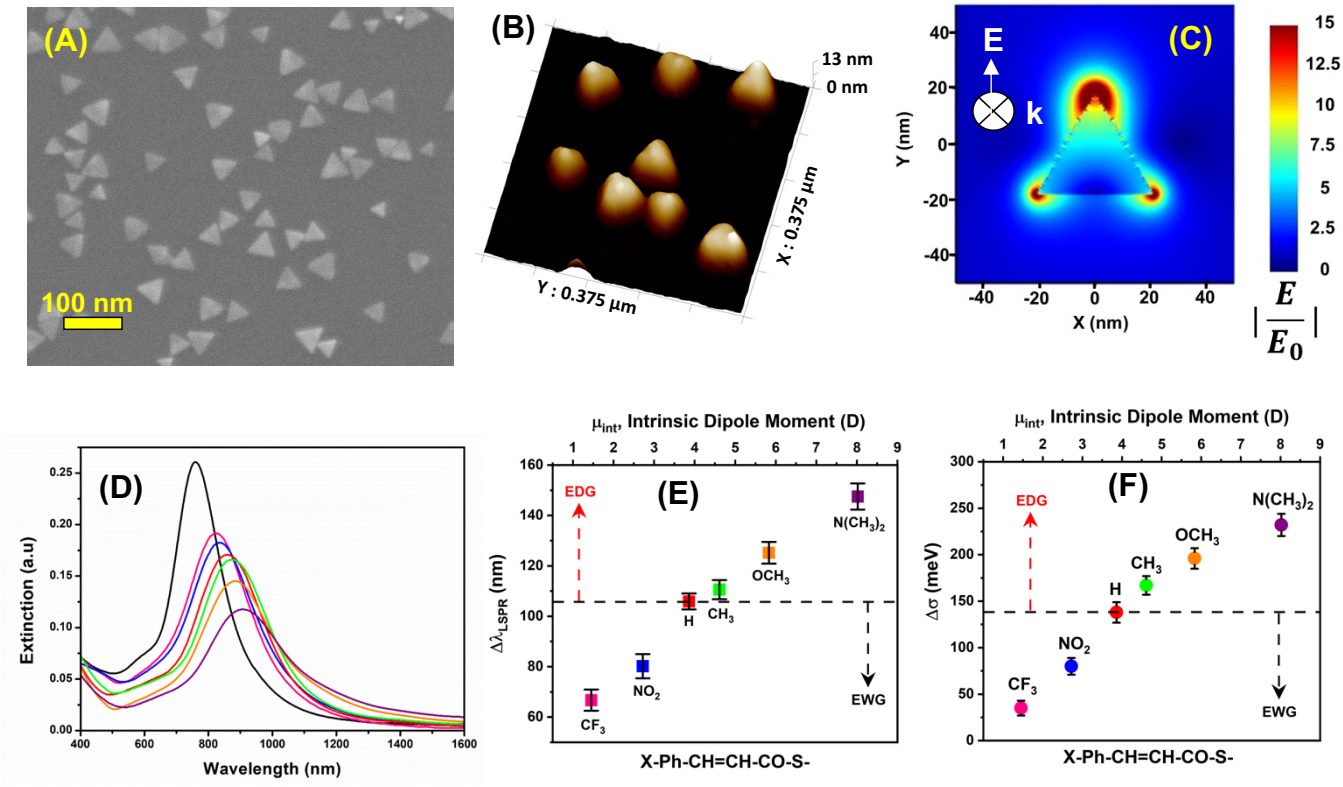


**Figure 1. (A)** SEM and **(B)** AFM image of TEA-passivated Au TNPs. **(C)** Finite domain time difference (FDTD) simulated electromagnetic field enhancement at 760 nm wavelength of 42 nm edge length Au TNP, as determined from SEM analysis, where maximum field enhancement occurs at the sharp edges and tips. Arrow indicates the direction of electric field. **(D)** Experimentally determined LSPR extinction spectra of Au TNPs TEA−passivated (black, 760 nm), and after TCA-X (X−Ph-CH=CH-CO−S−) functionalization: X = $CF_3$ (pink, 827 nm), X = $NO_2$ (blue, 840 nm), X = H (red, 865 nm), X = $CH_3$ (green, 871 nm), X = $OCH_3$ (orange, 886 nm), and X = $N(CH_3)_2$ (purple, 910 nm). **(E)** Representation of the observed LSPR shift [$\Delta\lambda_{LSPR} = (\lambda_{TCA\text{-}X} - \lambda_{TEA\text{-}Au\ TNPs})$] upon functionalization of Au TNPs with TCA-X ligands of different intrinsic dipole moments, which were determined in gas phase using DFT calculations. Red arrow indicates the $\lambda_{LSPR}$ shifts after functionalization with various electron donating groups (EDGs) and black arrow indicates the $\lambda_{LSPR}$ shifts after functionalization with electron withdrawing groups (EWGs) compared to when Au TNPs were functionalized with TCA-H. **(F)** Relationship between intrinsic dipole moment with change in the line width (FWHM, σ) of TNPs as a function of TCA-X ligands. Figure 2D, E, and F are color coordinated.

We performed Raman analysis to confirm the removal of original TEA ligands from the surface of TNPs and then functionalization with TCA-X ligands. Disappearance of the C-N Raman stretch of TEA at 1035 $cm^{-1}$ and appearance of the C-S and aromatic C=C

stretches at 1142 $cm^{-1}$and 1605 $cm^{-1}$, respectively, confirm the ligand exchange process (**Figure S3**). As illustrated in **Figure 1D**, an ~106 nm red-shift in LSPR dipole peak position of the TEA-passivated TNPs is observed after complete surface passivation with TCA-H. Interestingly, modification of the para-substitutions with strong electron withdrawing -$CF_3$ and strong electron donating -$N(CH_3)_2$ groups on the TCA-X ligands altered the magnitude of LSPR dipole peak shifts ($\Delta\lambda_{LSPR}$) differently. The -$CF_3$ and -$N(CH_3)_2$ substitutions produce $\Delta\lambda_{LSPR}$ of ~38 and ~44 nm blue and red shifts, respectively, versus X = H. **Figure 1E** summarizes the observed $\Delta\lambda_{LSPR}$ ($\lambda_{TCA\text{-}X-passivated} - \lambda_{TEA\text{-}passivated}$) upon surface modification of TEA-passivated Au TNPs with different TCAs. This is interesting because the magnitudes of the LSPR peak red-shifts follow the increasing order of electron donation, i.e., $\Delta\lambda_{CH3} < \Delta\lambda_{OCH3} < \Delta\lambda_{N(CH3)2}$. In contrast, the decreasing order of electron withdrawal i.e., $\Delta\lambda_{NO2} < \Delta\lambda_{CF3}$ results in blue shifting of the LSPR peak when we compare X = H attached to the ligands phenyl ring ($\Delta\lambda_H$). Since all the substituted TCAs have the same binding head group including thiolate, we would expect the lower energy $\lambda_{LSPR}$ red-shifts for -$CF_3$ or -$NO_2$ in comparison to -H. This is because, the classical Drude-Lorentz model implies that plasmon frequency ($\omega_p$) is expected to increase (decrease) [$\lambda_{LSPR}$ blue shift (red shift)] with increasing electron-donating (-withdrawing) ability of the para-substitution[23], as described by Eqs. 1 and Eq. 2, where $N_e$ is the free carrier (electron for Au) density, $m$ is the effective mass of an electron, $e$ is elementary charge, and $\varepsilon_0$ is the permittivity of free space.

$$\omega_p{}^2 = \frac{N_e\, e^2}{m\varepsilon_0} \qquad (Eq.1)$$

$$\omega_p \propto \frac{1}{\lambda} \qquad (Eq.2)$$

Furthermore, blue-shifts for electron donating -$CH_3$, -$OCH_3$, -$N(CH_3)_2$ groups are expected, however, we observe a completely opposite trend.

In addition to the change in the $\Delta\lambda_{LSPR}$, we observe a dramatic broadening – change in full-width at half-maximum, FWHM ($\Delta\sigma$) – of Au TNP dipole peaks, depending on X (**Figure 1F** and **Table S1**). Interestingly, the peak intensity is also reduced significantly as electron withdrawing functional groups were replaced with electron donating groups. Literature reports suggest that the refractive indices of most organic thiolate ligands share similar values[24], and the electron withdrawing ability of the sulfur atom barely influences the intensity of the LSPR peak and the $\Delta\sigma$ value of thiolate ligand-functionalized plasmonic metal NPs.[14] Therefore, we attribute this loss of scattering intensity ("plasmon damping") and very large changes in $\Delta\lambda_{LSPR}$ and $\Delta\sigma$, to delocalization of plasmon (coherently oscillated electrons) wavefunctions from Au TNPs into the interfacial hybrid MOs, where X group of TCA controls the magnitude of the delocalization process. If our argument of electron

wavefunction delocalization holds true then the $\lambda_{LSPR}$ position, which is controlled by free electron density ($N_e$, Eq. 1), and the resulting spectral area (oscillative strength) that is equal to the integrated peak, should be different among substituted TCAs.[25]

$$N_e = \sum Q \qquad (Eq. 3)$$

$$Q \propto \int \alpha_e(\nu) d\nu \qquad (Eq. 4)$$

Here, $Q$, $\alpha_e$, and $\nu$ denote the spectral area, the molar extinction coefficient, and the wavenumber ($1/\lambda$), respectively. The highest and lowest a spectral area of 35.4 and 22.5 are observed for -$CF_3$ and -$N(CH_3)_2$, respectively. The calculated spectral area for each TCA ligand is listed in **Table S2**. Thus, the decrease in spectral area from -$CF_3$ to -$N(CH_3)_2$ indicates an overall decrease of $N_e$ of Au TNPs.

It is also important to mention that we observe a large change in $\Delta\sigma$ ranging from 0.035 eV for TCA-$CF_3$ to 0.232 eV for TCA-$N(CH_3)_2$ (see **Figure 1F**). Our $\Delta\sigma$ value is significantly larger than those reported in the literature for Au NRs, which were functionalized with simple thiophenolate[16] or alkylthiolate ligands[14]. Previously, Link and coworkers reported ~0.040 eV $\Delta\sigma$ for alkylthiolate-functionalized Au NRs. There are two possible reasons that could lead to such a dramatic $\Delta\sigma$ value measured in our system: (1) The excited plasmon (coherent electron oscillation) due to light irradiation can decay via three major mechanisms: interband/intraband relaxation, radiation, and interface damping or surface damping. It has been reported that plasmonic NPs having one of their dimensions greater than 25 nm can undergo radiation damping.[26] In our case, the edge-length of TNPs is ~42 nm, thus they may encounter such damping. Furthermore, metal NPs displaying low plasmon energy (<1.8 eV, i.e., $\lambda_{LSPR}$ >688 nm) exhibit excited plasmon decay via non-radiative intraband relaxation.[27] (2) The surface of TNPs is atomically flat, thus it can allow TCA-X ligands to form a well-packed SAM resulting in the formation of more interfacial electronic states, which can act as interface damping channels of the surface plasmon resonance. We believe that the interface damping in TCA-Au TNP that is a part of delocalization of plasmon active electron wavefunctions is the major contributor in our system to account for the plasmon linewidth change which we discussed later in this article. Although we observe a significant increase in $\Delta\sigma$ value of TNPs due to the formation of TCA-X SAMs, they still maintain an excellent quality factor (Q) = $\lambda_{LSPR}$ (eV)/ $\Delta\sigma$ (eV), which defined as local-field enhancement,[27] is calculated to be ~42 and 6.0 for TCA-$CF_3$ and -$N(CH_3)_2$, respectively. Thus this previously unknown set of ligand-functionalized TNPs can serve as highly effective NPs for various plasmon-drive applications.

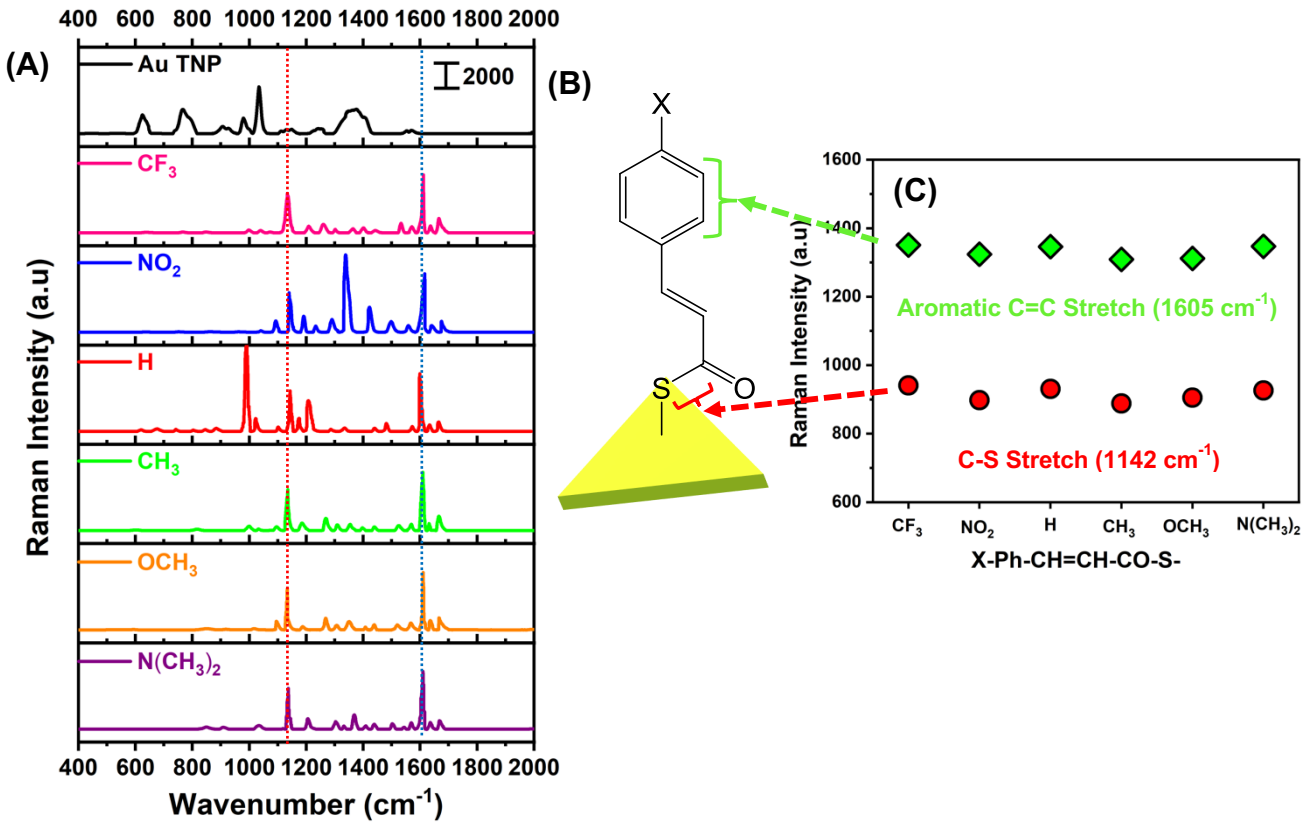


**Figure 2. (A)** Surface-enhanced Raman scattering (SERS)-based surface analysis of Au TNPs before (TEA-passivated, black) and after ligand exchange with TCA-X. The C-S, and aromatic C=C stretches are marked by red and blue dotted lines, respectively. **(B)** Schematic presentation identifying two important Raman stretches used for quantification. **(C)** SERS intensity of different TCA-X ligands attached onto Au TNPs for different vibrational modes: C-S (red spheres, 1142 $cm^{-1}$), aromatic C=C (green diamonds, 1605 $cm^{-1}$).

To rule out the possibility that it is not a variable ligand distribution (surface coverage) on the TNPs that produces the observed LSPR trend, we performed surface-enhanced Raman spectroscopy (SERS) measurements to determine the distribution of TCA in the SAM on the TNP surface. Previously, we demonstrated that TNPs were excellent SERS substrates for the quantification of various analytes, including covalently-attached thiolated ligands.[28, 29] **Figure 2A** shows the SERS spectra of Au TNPs passivated with TEA and after covalent functionalization with different TCA-X ligands. Observing the C-N Raman stretch at 1035 $cm^{-1}$ confirms the presence of TEA.[13] For the TCA-X-functionalized TNPs, we mostly focused on the appearance of the C-S and aromatic C=C Raman stretches at 1142 and 1605 $cm^{-1}$, respectively. As illustrated in **Figure 2B**, these two stretches will remain constant regardless of the functional group (X) attached to the phenyl ring in the TCA ligands. All TCA-functionalized TNP conjugates display nearly identical C-S and aromatic C=C stretches suggesting that the TCA surface coverage is more or less identical in the different SAMs (**Figure 2C**). Finally, we conducted marking experiments to determine the size and shape of Au TNPs before and after the TCA SAM formation. Silicon wafers containing etched

numerical markers were used to accurately determine the exact location on the surface. **Figure S4** depicts SEM images of Au TNPs with TEA passivation and after TCA-X (X = -H) functionalization. No apparent changes in the TNP shape are observed; specifically, the shape of sharp tips and edges remains same. The SERS and SEM data suggest that formation and morphology of SAMs from covalent attachment of TCA-X to TNPs do not contribute to the observed spectral trends in the $\lambda_{LSPR}$ and $\Delta\sigma$. Interestingly, $\Delta\lambda_{LSPR}$ and $\Delta\sigma$ trends closely follow the intrinsic dipole moment ($\mu_{int}$, gas phase dipole moment of computationally optimized geometry) of protonated TCAs (**Figure 1E,F**).

**Work function tuning in TCA-functionalized Au TNPs.** It has been shown that the chemical structure of organothiolate SAMs, particularly their resulting dipole moments, can significantly alter the work function ($\Phi$, in eV) of flat, bulk Au from the formation of a dipolar barrier as a consequence of covalent bond formation.[17-19, 30, 31] We are now poised to characterize the interfacial dipole effects on the $\Phi$ of TNPs as a function of altering groups (-X) of TCAs, which themselves can be considered to display dipole moment that can be approximated like a molecular rod. The $\mu_{int}$ of TCAs can be divided into two parts. The polar binding head group region (-S-C=O), and the aromatic backbone, which is substituted by different electron withdrawing and donating functionalities (X) that modulate the electron density and distribution within the entire molecule. Because all TCAs contain -S-C=O, the X group is expected to predominantly control the $\mu_{int}$ of our TCAs. Furthermore, the vinyl group connecting the terminal -S-C=O and phenyl ring should allow perpendicular orientation of the TCA attached onto the surface of TNPs causing plate-like symmetry and conformational flexibility to form densely packed SAMs.

Ultraviolet photoelectron spectroscopy (UPS) analysis is considered to be a highly sensitive technique to determine $\Phi$ of metals. The raw UPS secondary electron cut-off and valence band regions of different TCA-functionalized TNPs (shown in **Figure 3A and B**, respectively) are plotted by utilizing the UPS spectrum of pure Au foil (**Figure S5**). The work function of Au drops continuously from electron withdrawing to donating groups, and is much smaller than the original TEA-passivated Au TNPs (5.7 eV) as our reference. A similar trend is also observed if we consider the work function of clean Au surface of 5.12-5.25 eV as reported in the literature.[18, 19] Additionally, a 3.3 eV change in Au work function is observed through TEA passivation and SAM formation of TNPs (see **Table 1)**. To our knowledge, this is the largest change in Au work function upon formation of organothiolate SAMs.[12, 19] The presence of organothiolate SAMs via the formation of Au-S covalent bonds yields a range of $\Phi$ from that of clean, bulk Au(111) metal (5.5 eV) to ~3.3 eV versus vacuum.[17-19] Melosh and coworkers showed that tetramantane-containing thiol attachment reduces the $\phi$ of Au to 1.6 eV,[32] which is nearly the value previously reported for bulk Au when it was doped with a

monolayer of cesium.[33] Nevertheless, we report here the largest change in Au work function upon formation of organothiolate SAMs on an atomically flat surface of Au NPs (i.e., Au TNPs). Modulation of $\phi$ of bulk gold metal has been widely studied for the development of optoelectronic device fabrication. In contrast, we presented a large reduction of Au work function from 5.7 eV to 2.4 eV in a NP-organothiolate system, which can be considered as a functional plasmonics. **Table S5** summarizes the work function values of Au under various experimental conditions. We believe that the low work function of the Au TNP-TCA system could represent an excellent charge reservoir for various light-driven chemical transformations and/or electrode materials for optoelectronic device fabrication.

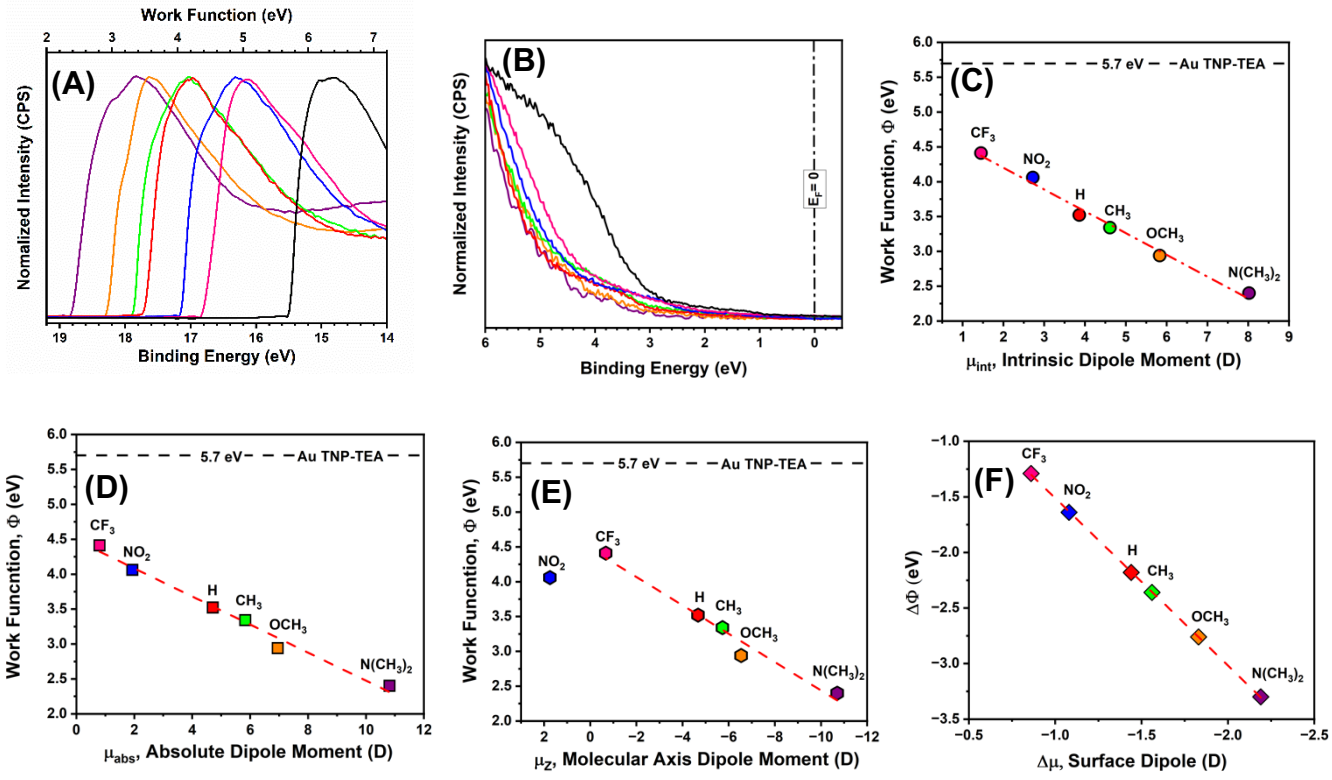


**Figure 3. (A)** Secondary electron cut-off region of UPS spectra used to determine the work function (Φ) of TCA-X-functionalized Au TNPs: X= TEA (black), p−$CF_3$(pink), p−$NO_2$ (blue), p−H (red), p−$CH_3$ (green), p-$OCH_3$ (orange), and p−$N(CH_3)_2$ (purple). **(B)** Valance band edge region of photoelectron spectra. The dotted line in Figure **(B)** represents the Fermi energy level ($E_F$) set to 0. **(C)** Dependence of the work function Φ (from UPS analysis) on computationally determined gas phase dipole moment (intrinsic dipole moment, $\mu_{int}$) of free TCA-X (slope= -0.31 eV/D); **(D)** absolute dipole moment ($\mu_{abs}$) of X-TCA-$Au_3$ (slope= -0.20 eV/D), **(E)** molecular axis dipole moment ($\mu_z$). **(F)** Change in work function [$\Delta\Phi = (\Phi_{TCA\text{-}X} - \Phi_{TEA\text{-}Au\ TNPs})$] was plotted against mathematically calculated surface dipole ($\Delta\mu$) created at the surface of the metal-ligand interface (interfacial dipole) (slope= 1.50 eV/D). All the dipole moments were calculated in gaussian-16 using density functional theory (DFT) calculations optimizing the model geometry with B3LYP and BP86 hybrid functionals in gas phase when Au atoms were present and absent, respectively and 6-311+G** basis set for all atoms except gold. LANL2DZ basis set was used for gold atoms. The color scheme here is coordinated as described in **Figure 3A-F.**

**Table 1:** Work function determination and calculated different dipole moments of TCA-X ligands

| X-Ph-CH=CH-CO-S-X= | High Energy Cut Off (eV) | Work Function, Φ (eV) | ΔΦ (eV) | Δμ, Surface Dipole (D) | $\mu_{int}$ (D) | $\mu_{abs}$ (D) | $\mu_z$ (D) |
|---|---|---|---|---|---|---|---|
| Au TNP-TEA (black) | 15.50 | 5.70 | - | - | - | - | - |
| p-$CF_3$ (pink) | 16.79 | 4.41 | -1.29 | -0.86 | 1.45 | 0.80 | -0.67 |
| p-$NO_2$ (blue) | 17.12 | 4.08 | -1.62 | -1.08 | 2.72 | 1.93 | 1.75 |
| p-H (red) | 17.73 | 3.47 | -2.23 | -1.48 | 3.86 | 4.71 | -4.67 |
| p-$CH_3$ (green) | 17.86 | 3.34 | -2.36 | -1.57 | 4.61 | 5.83 | -5.74 |
| p-$OCH_3$ (orange) | 18.26 | 2.94 | -2.76 | -1.83 | 5.83 | 6.95 | -6.54 |
| p-$N(CH_3)_2$ (purple) | 18.80 | 2.40 | -3.30 | -2.19 | 8.02 | 10.81 | -10.70 |

We find that the Φ of Au depends linearly on the $\mu_{int}$ of X with a best-fit slope of -0.31 eV per Debye (**Figure 3C**). The work function of Au also follows linearly with absolute dipole moment ($\mu_{abs}$) of ligand-functionalized TNPs. The $\mu_{abs}$ for each TCA was calculated through DFT calculations modelling the TCA-$Au_3$ system, where each S atom is bound to three Au atoms[34] yielding a slope of -0.20/Debye (**Figure 3D**). We believe this difference in slope between $\mu_{int}$ and $\mu_{abs}$ is related to the molecular orientation of TCA with respect to the TNP surface, more specifically from the difference in interface dipoles. We assume that molecular backbone of TCA molecules in the SAM are present in a perpendicular orientation to the surface where $\mu_z$ is the molecular dipole along the z axis (**Figure S6**). As shown in **Figure 3E**, the effective work function value of Au changes linearly from highly electron withdrawing (-$CF_3$) to highly electron donating (-$N(CH_3)_2$) groups with a slope of -0.20/Debye. It is important to note that the work function data for -$NO_2$ deviate from the linear slope. As we determined that the surface density of all the TCA ligands onto TNPs is same within the experimental error, the polarization effects of charge termini may influence the interfacial dipole (also known as surface dipole or surface induce dipole) in tightly-packed SAMs.[35-37] In our system, the -$NO_2$ has partially charged atoms, therefore, it is possible that intermolecular charge interactions dissipate the dipole field and lower the overall interfacial dipole. Such behaviour may explain our observed smaller $\Phi/\mu_z$ and/or $\Phi/\mu_{abs}$ versus $\Phi/\mu_{int}$. Interestingly, except for -$NO_2$, the DFT-calculated $\mu_z$ values for other TCAs are negative. This negative $\mu_z$ represents charge pointing out from the Au-to-ligand moiety. This is the first evidence of our central hypothesis that the electron wavefunction of Au is extending from the Au core boundary into ligand backbone, which we refer as delocalization of electron wavefunctions, making the Au-S interface like a parallel plate capacitor where partial positive and negative charges reside on the Au and ligand, respectively.

We next sought to investigate the change in work function ($\Delta\Phi$) of Au caused by the formation of TCA SAMs as a function of X by utilizing the parallel capacitor model,[38]

$$\Delta\Phi = \Phi_{\mathrm{SAM}} - \Phi_{\mathrm{TEA}} = \frac{\Delta\mu . e}{\varepsilon_0 A} \qquad \text{(Eq.5)}$$

where $\Delta\mu$ is the SAM/TCA-X-induced interfacial dipole, and *A* is the surface area of a thiolate. **Figure 3F** illustrates the value of $\Delta\Phi$ and $\Delta\mu$ calculated using Eq. 5 as a function of X that shows a tight linear fit with a slope of 1.50 eV/Debye. Phenomenologically, the interfacial dipole appears to be nearly four-fold lower in magnitude than the $\mu_{abs}$ or $\mu_{int}$ (**Table 1**). This is not surprising because the charge distribution at the metal-ligand interface within the SAM allows the dipole field to dissipate, thus the effective value of the interfacial dipole is always lower than the molecular dipole of a free ligand.[39, 40] This is because charge ordering and distribution take place from formation of a chemical bond between metal and ligand, such as Au-S in the current system. Taken together, the directionality of interfacial dipole strongly supports the observed LSPR red-shifts in TCA-functionalized Au TNPs.

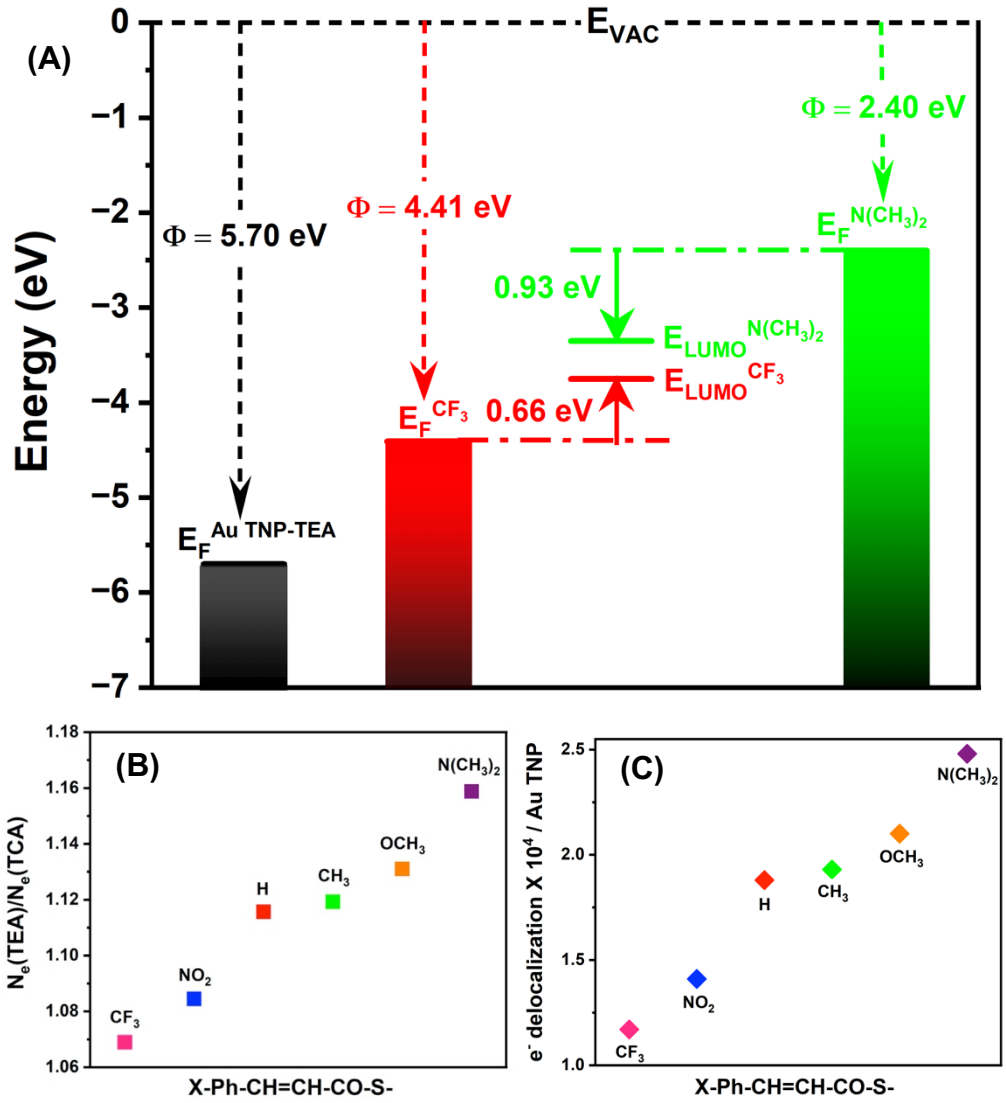

**Figure 4. (A)** Schematic diagram of the proposed electron wavefunction delocalization between the Fermi level ($E_F$) of Au TNP and the LUMO ($E_{LUMO}$) of TCA-X-functionalized $Au_3$, where X = $N(CH_3)_2$, and $CF_3$ are represented in green and red, respectively. Fermi level energies were determined from UPS analysis, whereas energies of hybrid LUMOs were determined through (DFT) calculation in VASP. Work function (Φ) values are indicated with respect to the vacuum level ($E_{vac}$) for para substituted X-Ph-CH=CH-CO-S-functionalized Au TNPs. **(B)** The ratio of free carrier density of TEA-passivated Au TNPs ($N_e$(TEA)) and after ligand exchange chemistry with TCA-X ligands ($N_e$ (TCA)). **(C)** Calculated number of electrons wavefunction delocalization per TNPs upon functionalization with TCA-X ligands. The color scheme here is coordinated with the recorded LSPR spectra as in **Figure 2D**.

**Mechanisms underlying the modulation of plasmonic properties.** We have found that for TCA-functionalized Au TNPs, electron withdrawing (-$CF_3$ and -$NO_2$) and donating (-$CH_3$, -$OCH_3$, -$N(CH_3)_2$) groups provide LSPR blue and red-shifts, respectively, versus -H. In order to explain these unusual plasmonic properties, we took advantage of the molecular orbital (MO) approach to examine the Au-TCA interfacial electronic states. In the following, we will consider the electronic effects arising from energy level alignment between metal and ligand, and the hybrid interfacial electronic states from a thermodynamic viewpoint. UPS data provide a solid method to determine the Au $E_F$ for different ligand functionalization. **Figure 4A** shows the relevant energy level diagram based on our UPS measurements and DFT-calculated HOMO and LUMO positions of different ligands (-X). **Table S3** provides the value of gas-phase HOMOs and LUMOs of free TCA ligands and the TCA-$Au_3$ system (hybrid MOs'). For the simplicity, we discuss the results based on two functional groups, i.e., -$CF_3$ and -$N(CH_3)_2$ because: (1) -$CF_3$ and -$N(CH_3)_2$ are very strong electron withdrawing and donating groups, respectively, and (2) they provide the most extreme LSPR shifts in our functionalized TNPs (**Figure 1**). For Au TNPs with TCA-$CF_3$ and -$N(CH_3)_2$ containing SAMs, the work functions are reduced to 4.41 and 2.40 eV, respectively, from TEA-passivated TNPs (Φ = 5.7 eV). Upon attachment of TCA to Au, hybrid HOMOs and LUMOs will form at the metal-organic interface. Empty LUMOs' for -$CF_3$ and -$N(CH_3)_2$-functionalized Au are calculated to be at -3.75 and -3.33 eV, respectively, *versus* vacuum. Therefore, at the steady-state, more thermodynamically favourable electron wavefunction delocalization is expected to take place for TCA-$N(CH_3)_2$-SAM modified Au TNPs than for TCA-$CF_3$ ligands and other ligands studied in this work. Considering that 9 nm TNP is a plasmonic slab, the energy of LSPR-active electrons would be ~ -3.3 eV versus vacuum.[41] This energy value resides above the empty LUMO' of TCA-$CF_3$-SAM modified TNPs, allowing favourable electron transfer/electron wavefunction delocalization. Noticeably, TCA-$NO_2$ also allows similar electronic effects in the current system (**Figure S7**). Electron transfer/wavefunction delocalization results in a decrease in free electron density in Au TNPs, and according to the Drude model (to Eq. 1 and 2), under such circumstances, we should expect an LSPR red-shift of the plasmon dipole peak of Au TNPs. Taken together, our electronic energy level

diagram suggests that even electron donating functional group covalently attached to plasmonic nanostructures via thiolated organic ligands can trigger transfer of free electrons from metal into the ligand moiety.

We postulate that in this current system, LSPR red-shift of Au TNPs upon functionalization with TCAs occurs due to the delocalization of Au electron wavefunctions and not direct/indirect transfer of Au electrons from $E_F$ to the hybrid LUMOs'. The later transfer mechanism is explicitly studied as the CID effect, which is a plasmon damping pathway where complete transfer of metal hot electrons to the MOs (mainly LUMOs) of passivating ligands .[14-16, 42] Herein, we consider that the electrons reside at/or below the $E_F$, behave as valance electrons, and allow their wavefunctions to be delocalized at the interfacial hybrid MOs ("partial electron transfer"). To better understand the mechanism, we calculated the $N_e$ values for different TCAs from our ensemble optical measurements and determine the $N_e$(TEA)/$N_e$(TCA) ratio (see **Figure 4B**, and **Table S4**). To determine the $\omega_p$ from the Drude-Lorentz model, we utilized an appropriate shape factor for the two-dimensional shape of TNPs.[43] All the information is provided in the **Supporting Information** file. As shown in **Figure 4C**, delocalization of wavefunction equivalent to 1.2-2.5 x $10^4$ electron /TNP take place depending on the ligand type. The free carrier density of Au is ~$10^{22}$ $cm^{-3}$,[44] and during the light exposure ~$10^5$ electrons can be excited near the $E_F$ for a 40 nm plasmonic Au platelet.[45] Therefore, it is reasonable to take into consideration that an ~$10^5$ electrons involved in the delocalization process. Nevertheless, considering all the faces of a TNPs exposed for TCA functionalization (except the bottom flat surface, which is attached to the silanized glass surface), ca. 6000 TCA/TNP can be attached (**Figure S8**). Therefore, ~3.2 electrons/ligand are transferred from Au-to-hybrid LUMOs', possibly within LUMO, LUMO+1 and LUMO+2 orbitals to accommodate such a larger charge. To the best of our knowledge, Lomaner et al.,[35] previously reported the highest metal-to-ligand charge transfer of 1.8 electrons/ligand. Instead of the wavefunction delocalization, transfer of electrons from $E_F$ to hybrid LUMOs' will result in formation of holes and any uncaptured holes will slowly degrade the TNPs. Although Au is extremely stable under such circumstances, the Au-S bond tends to oxidize if holes are easily accessible. This will result in alteration of plasmonic properties. We observe that the plasmonic properties (LSPR peak position, intensity and FHWM) of TCA-functionalized Au TNPs are stable for at least a week when the coverslip-bound, X-TCA-functionalized TNPs were stored under $N_2$ atmosphere (**Figure S9**). Moreover, once the electrons are transferred into hybrid LUMOs', the electrons are expected to move within the aromatic ring, thus afterwards molecule-to-metal charge transfer is highly unlikely to occur. In contrast, the delocalization (partal transfer) allows sharing of electron density between metal and ligand conjugates. Therefore, we can expect that changes in the SAM structure would allow retraction of the electron wavefunction within

the metal and thus influence the plasmonic properties. More specifically, we should be able to observe reversible plasmonic properties if one type of TCA ligand on the TNP surface is replaced by a second (different one) through a solid-state ligand exchange reaction (*vide infra*).

So far, we have discussed the importance of interfacial energy levels of metal-ligand hybrid conjugates where the energy of hybrid MOs' are mostly controlled by the interfacial dipole moment. Herein, we show the vinyl conjugation (double bond) connecting -S-C=O with the benzene ring also plays a major role in the wavefunction delocalization process. As shown in **Figure S10A,B**, a SAM of -SCO-CH-CH-Ph-H produces a 47 nm red-shift of $\lambda_{LSPR}$, which is 58 nm smaller than the -SCO-CH=CH-Ph-H-SAM modified TNPs (TCA-H, $\Delta\lambda_H$ =105 nm). The $\mu_{int}$ of ligands without and with vinyl conjugation are 1.86 and 3.86 Debye, respectively. As we observed before, the higher the $\mu_{int}$, the larger the $\Delta\lambda$ value (**Figure 1D**). Therefore, it can be argued that the vinyl conjugation influences the work function values differently and thus the interfacial electronic states, resulting in observation of a smaller $\lambda_{LSPR}$ for -SCO-CH-CH-Ph-H SAMs. We prepared a different SAM using -SCO-CH-CH-Ph-N$(CH_3)_2$ ligands, which themselves have a $\mu_{int}$ of 3.82 Debye that is nearly identical to -SCO-CH=CH-Ph-H (TCA-H). Interestingly, we observe an ~30 nm smaller $\Delta\lambda$ value for -SCO-CH-CH-Ph-N$(CH_3)_2$ in comparison to TCA-H. This result indirectly suggest that the presence of the vinyl group is important for the delocalization process where electron wavefunctions can leave the TNP boundary into interfacial orbitals, and then further extend through the entire $\pi$-conjugated aromatic structure. This result is in agreement with the literature where extension of wavefunctions of lithographically-prepared Au nanorods was observed due to the presence of surface attached conjugated polymers.[46] Finally, we tested varying the position of functional group in the aromatic ring and its influence on the plasmonic properties. The SAM of para- ($\mu_{int}$ = 2.72 Debye) and meta-$NO_2$ ($\mu_{int}$ = 2.64 Debye) substituted TCA display almost identical values, whereas para- ($\mu_{int}$ = 5.83 Debye) and meta-$OCH_3$ ($\mu_{int}$ = 6.41 Debye) substituted TCA provide slightly different plasmonic responses (see **Figure S10C,D**) Together, we suggest that the delocalization of electron wavefunctions is the most probable mechanism as opposed to the CID mechanism, where not only the interfacial dipole moment but also the vinyl conjugation play critical roles in modulating the plasmonic properties of our TCA-functionalized Au TNPs. Specifically, conjugated structures facilitate the propagation of electron wavefunction to a longer distance, resulting in larger red-shifts in comparison to non-conjugated ligands.

**Shape-dependent optoelectronic properties of TCA-X-functionalized Au NPs.** To examine effect of the TCA-X ligands on the optoelectronic properties of Au NPs as a function

of shape, we further functionalized Au nanospheres (Au NSs) and Au nanorods (Au NRs) with two TCA-X ligands, where X = -H and -$N(CH_3)_2$. We selected these ligands because TCA-H is our reference ligand, and TCA--$N(CH_3)_2$ produced the largest LSPR shifts and the largest change in Au $\phi$ for triangular nanoprisms (TNPs). ***Figure 5A,B*** *show the* SEM images of chemically-synthesized ~40 nm diameter Au NSs, and 45 nm long and 15 nm diameter NRs attached onto silanized glass coverslips. We selected these dimensions of NSs and NRs so that their optoelectronic properties can be compared with ~42 nm edge-length Au TNPs. Glass substrate-bound Au NSs display $\lambda_{LSPR}$ at ~520, whereas the longitudinal peak of NRs appears at 700 nm in air (**Figure 5C**). We observe that the $\Delta\lambda_{LSPR}$ for NSs and NRs upon functionalization with TCA-H and TCA-$N(CH_3)_2$ follows the same trend as determined for TNPs where - $N(CH_3)_2$ provides higher $\Delta\lambda_{LSPR}$ values than -H. The most noticeable plasmonic property that can be observed is that the magnitude of the $\Delta\lambda_{LSPR}$ value is much smaller for NSs (~17 nm) and NRs (~55 nm) as compared to TNPs (~150 nm) for TCA-$N(CH_3)_2$, which provides the largest change in $\Delta\lambda_{LSPR}$ value (see Figure 1D,E). According to the "lightning rod effect",[47] the electric field is expected to be more highly concentrated at the tips of prolate ellipsoids (here approximating rods and triangular prisms) than spherical particles, which only display uniform polarization. The FDTD-simulated electromagnetic field enhancements for a single Au NS and NR are shown in **Figure 5D,E**, which is in agreement with the lightning rod effect. Therefore, we believe that observed relatively small change in $\Delta\lambda_{LSPR}$ value is due the differences in electromagnetic field enhancement from sharp tip- and corner-containing TNPs in contrast to non-sharp curvatures in the NRs and NSs. Nevertheless, the magnitude of $\Delta\lambda_{LSPR}$ value for Au NSs upon functionalization with conjugated aromatic thiolate ligands is agreement with the literature.[24] In contrast, our $\Delta\lambda_{LSPR}$ value for unsubstituted TCA-functionalized Au NRs is significantly higher than previously reported, aliphatic carboratethiolate-modified[15] and alkylthiolate-functionalized Au NRs.[48] We believe vinyl conjugation, along with the aromatic ring allows better plasmon electron wavefunction delocalization than aliphatic thiolate-functionalized NRs where only CID effects affects the LSPR peak shift.

We determined $\phi$ value of Au for NSs and NRs that are functionalized with TCA-H and -$N(CH_3)_2$. As illustrated in **Figure 5F-H**, the $\phi$ for NSs and NRs are 4.33 and 4.28 eV for the TCA-H ligand, respectively, whereas relatively lower $\phi$ values are measured for the TCA-$N(CH_3)_2$ ligand. Importantly, $\phi$ values for NS and NRs are in close proximity to the literature data for the thilolated ligand-functionalized bulk Au surface,[18, 19, 49] but significantly lower than Au TNPs. It is know that the packing density of ligands can create different surface polarizabilities in the NPs forming dipole-like electrostatic asymmetry.[50] We believe that the

non-centrosymmetric electrostatic surface potential creates dipole asymmetry in Au TNPs, and probably NRs that is critical for the generation of surface dipoles and resulting modulation of $\phi$ upon functionalization of NPs with dipolar ligands. Au TNPs contain a larger number of sharp tips and edges as compared to NRs, thus it is expected that TCA-functionalized TNPs will produce larger surface dipoles and lower $\phi$ for Au. In contrast, Au NRs with non-sharp curvature at the ends and the preferential attachment of thiolated ligands on the Au (111) facet at the end[51, 52]creates surface dipoles, but expected to be lower compared to TNPs, resulting in less dramatic modulation of the $\phi$ for NRs. For spherical NSs, the symmetry of the surface charge density will sum to a net zero dipole, and thus ligand dipole moment is the only contributing factor to change the metal-ligand interfacial dipole moment similar to thiolated ligand functionalized bulk Au.[17-19] In other words, the energy difference between the Fermi of TCA passivated Au NRs and LUMO of the hybrid system would not be much higher than as is observed for TCA-passivated TNPs, which is indeed reflected in the plasmonic shift observed for Au NRs. To correlate the LSPR shift and $\phi$, as part of working model (**Figure 4A**), it is clear that the energy differences between (1) $E_F^{(NR)}$ and $E_{LUMO}^{N(CH3)2}$, and (2) $E_F^{(NS)}$ and $E_{LUMO}^{N(CH3)2}$ are too large for facile delocalization of surface plasmon-active electrons from $E_F^{(NR)}$($E_F^{(NS)}$) to $E_{LUMO}^{N(CH3)2}$, and thus there is a relative small response of the overall plasmonic properties of TCA-X ligand-functionalized Au NSs and NRs. Taken together, the data presented above are intriguing and suggest that the shape of plasmonic metal NPs substantially modulates the work function when organic thiols are covalently attached onto them.

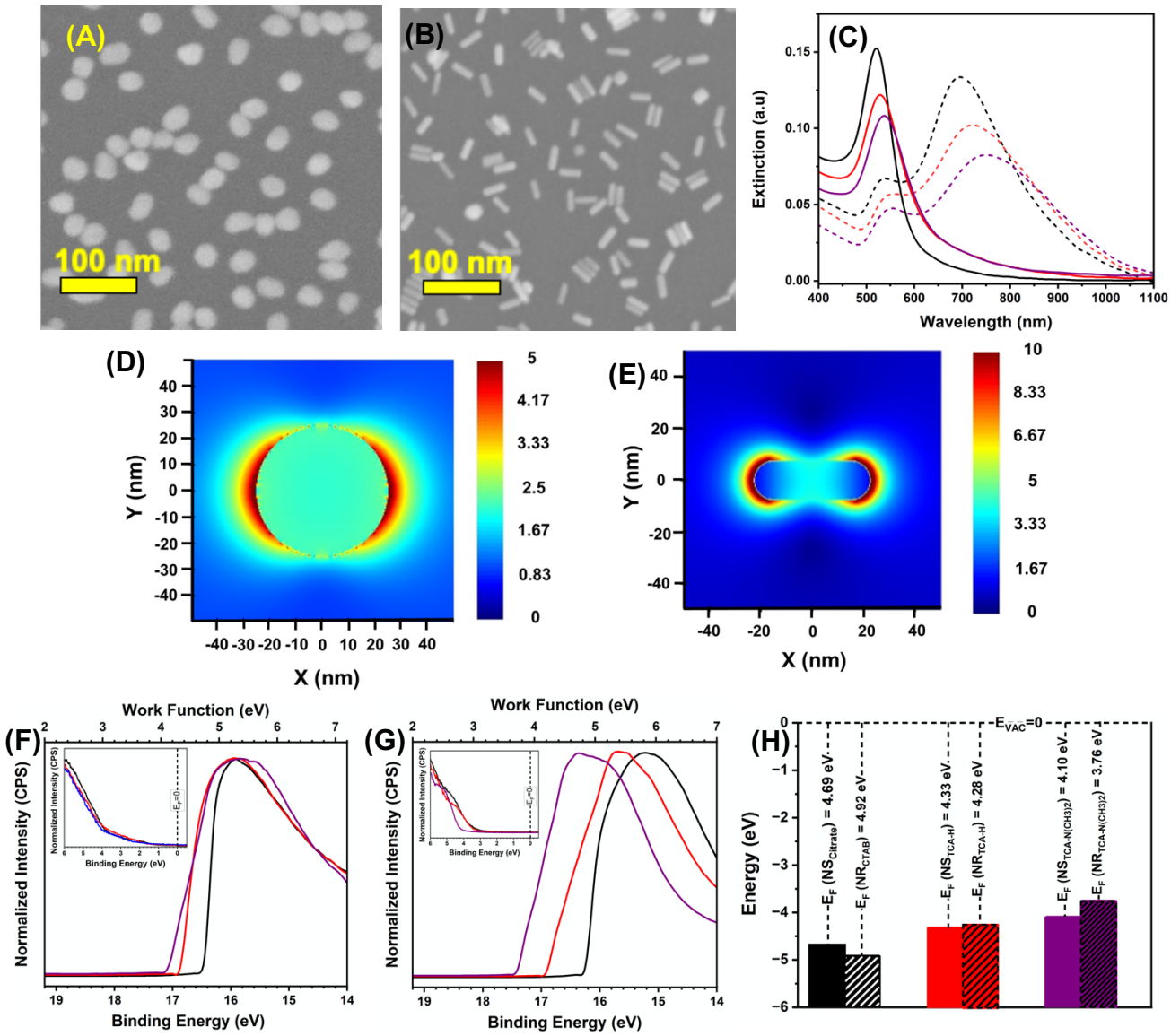


**Figure 5.** SEM images of Au NSs and NRs attached onto a silanized glass substrate before TCA-X modification. (C) Experimentally determined LSPR extinction spectra of citrate-stabilized Au NSs (solid curve) (black, 520 nm) and after TCA-X functionalization: X = H (red, 530 nm), X = $N(CH_3)_2$ (purple, 537 nm), and CTAB-coated Au NRs (dash curve) (black, 700 nm) and after TCA-X functionalization: X = H (red, 726 nm), and X = $N(CH_3)_2$ (purple, 755 nm). Figure panels are color coordinated with the recorded LSPR spectra as in **Figure 2D**. The extinction spectra were recorded in air. FDTD simulated electromagnetic field enhancement at 520 nm wavelength of a 40 nm diameter Au NS (D), and a 40 nm long and 15 nm diameter Au NR (E). Arrow indicates the direction of electric field. Secondary electron cut-off region of UPS spectra used to determine the work function (Φ) of TCA-X-functionalized **(F)** Au NSs (black) and **(G)** Au NRs (black): X= p−H (red), and p−$N(CH_3)_2$ (purple). The inset of (F) and (G) shows the valance band edge region of the nanostructures. The dotted line in valance band edge region represents the Fermi energy level ($E_F$) set to 0. **(H)** Schematic representation of calculated Fermi energy value with respect to the vacuum energy ($E_{vac}$) for TCA passivated Au NSs (solid bars) and NRs (broken bars). The graphical representations are color–coordinated with respect to the corresponding UPS spectra.

**Surface ligand chemistry-controlled modulation of interfacial electronic structures.** Our proposed mechanism of electron wavefunction delocalization depends on the electronic interactions at the interface of the metal-organic hybrid system. Next, we theoretically modelled the interaction and electronic structures near the $E_F$ of the system by characterizing the DOS of hybrid electronic orbitals that participate in the delocalization process from the metal to the ligand. A 4x4 Au slab was designed as our model with an Au (111) facet attached to one TCA ligand forming an Au-S bond (**Figure 6A**). We used one ligand on the slab In the plane wave-based DFT calculation to avoid intermolecular interactions. Although some differences are observed in our TCA-Au metal-organic hybrid interface model, the total DOS (TDOS) for the three different functionalities, i.e., $-CF_3$, -H. and $-N(CH_3)_2$ are nearly identical (**Figure 6B**). This could be due to contribution of a large number of d-bands in the TDOS. Expanding the TDOS ($|E-E_F|$= 3.0 ev) (**Figure 6C**), we clearly observe a marked difference in the available density of electronic states. We have also observed that further expansion of the TDOS very close to fermi level ($|E-E_F|$=0.2 ev) (**Inset of Figure 6C**) causes available DOS to increase from $-CF_3$, to -H, to $-N(CH_3)_2$ for TCAs. A higher DOS should promote a large number of delocalized wavefunctions. The data support our proposed mechanism of enhanced delocalization of electron wavefunction for $-N(CH_3)_2$ compared to $-CF_3$, therefore showing maximum plasmonic response for $-N(CH_3)_2$ over $-CF_3$, while -H appears in between.

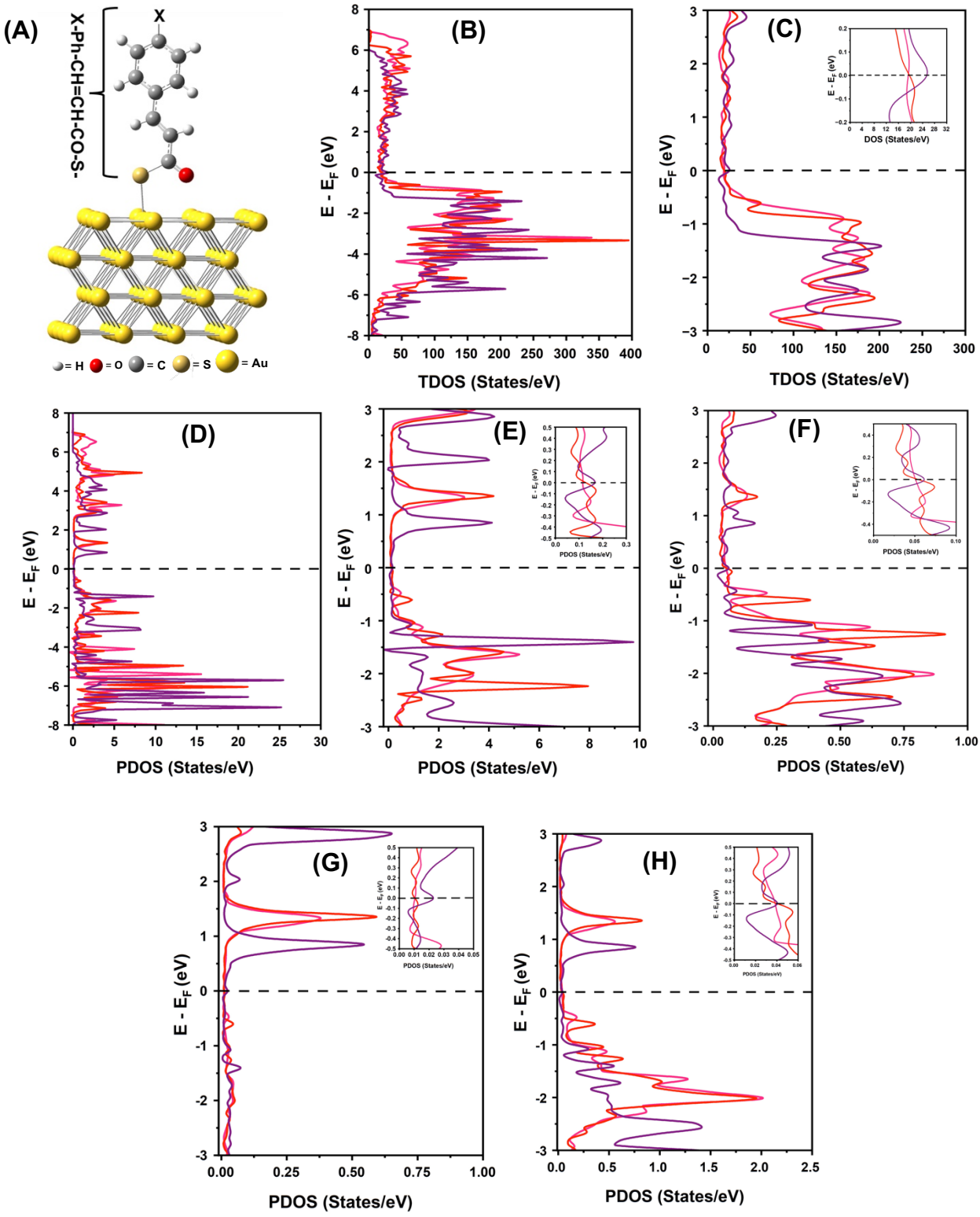


**Figure 6. (A)** Schematic of a computationally optimized 4x4 slab of Au (111) containing a single TCA-X ligand. **(B)** Total DOS (TDOS) values of the whole atomic model of TCA-X attached to the gold slab; where X= $CF_3$ (pink), H (red), $N(CH_3)_2$ (purple). **(C)** Expanded total DOS (TDOS) values in the range of -3 to +3 eV. The inset shows the TDOS near the Fermi level ($E-E_F=0$). **(D)** Projected DOS values (PDOS) for only TCA-X ligands; where X= $CF_3$ (pink), H (red), $N(CH_3)_2$ (purple). **(E)** Expanded PDOS values projected for the ligand in the range of -3 to +3 eV. The inset shows the PDOS for the

ligand near the Fermi level (E-$E_F$=0). PDOS values projected for the individual sulfur atom **(F)**, the individual carbon atom of the carbonyl group attached to sulfur atom **(G)**, and carbonyl oxygen atom **(H)** are expanded in the range of -3 to +3 eV. Insets of (F)-(H) show PDOS values near the Fermi level.

All the TCA ligands have the same basic structures, except for variation in their electronic substitutions at the para position of the aromatic ring. As a result, the projected DOS (PDOS) plots for the TCAs show similar distributions of electronic states in the range of -8 to +8 eV (**Figure 6D**). Expanding the PDOS for the above-mentioned three ligands (**Figure 6E**), we can observe the highest hybrid electronic states of -$N(CH_3)_2$ near the $E_F$, then -H, followed by -$CF_3$, (inset of **Figure 6E**). This difference in the PDOS is important because it arises mainly from variation in the chemical interaction at the Au (111) surface caused by the characteristics of the substitutions in the ligand aromatic ring. This difference indicates the crucial role wavefunction delocalization plays in enhancing the probability of finding residual free electrons in the electronic states near the Fermi level at the interface, and also promoting the red-shift of plasmonic oscillations. Furthermore, we calculated the PDOS for individual atoms in the TCA structure, specifically S, C, and O that are present as part of the bonding motif (-S-C=O). **Figure 6F** illustrates the PDOS of S where in order, highest to lowest distributions of electronic states are observed for -$N(CH_3)_2$, -H, and -$CF_3$. This result is agreement with the TDOS data and suggest that although each different ligand forms a covalent Au-S bond, the distribution of electronic states near the $E_F$ is controlled by the X group. PDOS for the carbonyl carbon atom, that is in direct covalent attachment to the S atom also follows similar PDOS result as S (**Figure 6G**). Although, the overall PDOS determined for the carbonyl oxygen atom for these three substituents are different, expanding the PDOS for the O atom near the $E_F$ appears to show the DOS crossover at a single point at the E-$E_F$ Fermi level (**Figure 6H**). Therefore, we believe that the carbonyl O is neither involved in bonding with the Au surface nor has direct attachment with the anchoring S atom. Together, our results confirm an unusual characteristic of the Au-S covalent bond, which is controlled by the X group in (1) constituting the metal-ligand hybrid interface, (2) promoting the variable degree of delocalization of $E_F$ level electron wavefunctions, and (3) modulating the plasmonic properties of TCA-functionalized Au TNPs.

**Reversible tuning of plasmonic properties:** As schematically demonstrated in **Scheme 2**, we conducted a complete set of ligand exchange chemistry experiments to characterize the reversible tuning of the plasmonic properties of TCA-functionalized Au TNPs in the solid-state. Since Au TNPs display maximum influence of their optoelectronic properties upon TCA-X ligand functionalization, we limited our reversibility study on this particular shape. We started with TEA-passivated TNPs and then functionalized with TCAs (X = -H), which yields a $\Delta\lambda_{LSPR}$ red-shift of 104 nm. After further exchanged with -$N(CH_3)_2$ we observe a red shift of

$\Delta\lambda_{LSPR}$ of 42 nm. Therefore, this two steps exchange show 146 nm red-shift that is similar to the single step ligand exchange of TEA-passivated TNPS with X = -$N(CH_3)_2$. (**Figure 1D**) A $\Delta\lambda_{LSPR}$ blue shift of 65 nm is observed when -$N(CH_3)_2$ was exchanged with $NO_2$. Finally, a 23 nm red shift is observed upon replacing -$NO_2$ with -H. Fully reversible LSPR peak position shits are also achieved by exchanging -H with -$NO_2$ followed by -$N(CH_3)_2$ (see **Figure S11**). **Figure 7A** shows representative LSPR spectra of Au TNPs upon sequential ligand exchange reactions with various TCAs. A summary of the change in $\lambda_{LSPR}$ in each step of sequential ligand exchange process is shown in **Figure 7B**. The overall plasmonic responses for different exchange sequences of TCA-functionalized Au TNPs follow the above-mentioned electron wave function delocalization model. We believe that the exchange of a particular type of ligand with a second ligand in the SAM alters the Au-TCA interfacial dipole moment, resulting in the formation of energetically different HOMOs and LUMOs than found in the parent ligands. Therefore, the $\Delta\lambda_{LSPR}$ value is dictated by the chemical structure of the surface passivating ligands. Overall, the ~90 nm reversible tuning of $\lambda_{LSPR}$ is the largest value reported to date for plasmonic metal nanostructures.[13, 53]

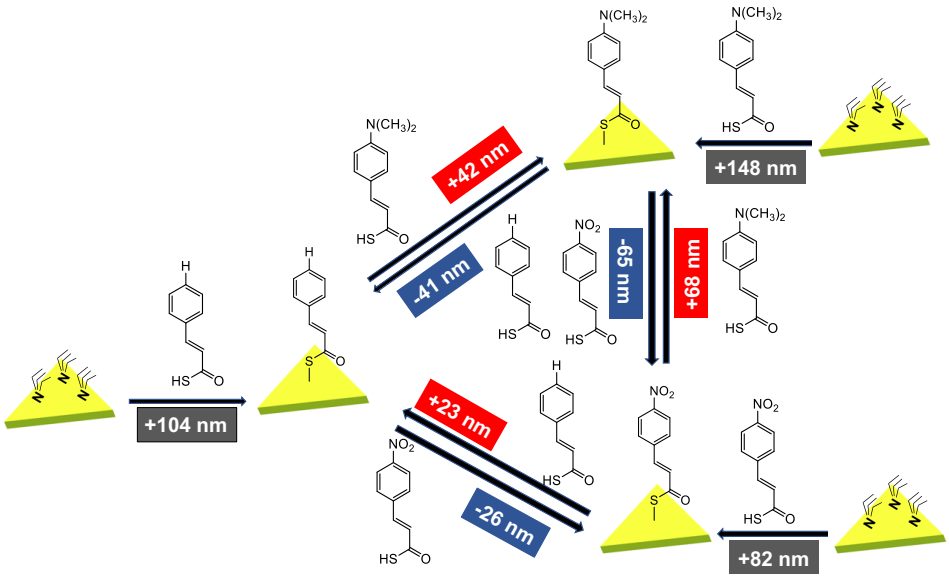


**Scheme 2.** Schematic representation of ligand-controlled reversible modulation of LSPR properties of Au TNPs using various TCA-X ligands. Blue and red boxes represent the value of the $\lambda_{LSPR}$ blue shift and red shift, respectively, upon ligand exchange in a subsequent step. Gray boxes represent the value of $\lambda_{LSPR}$ when ligand exchange chemistries were performed on TEA-passivated Au TNPs with TCA-X ligands. For simplicity, a single TCA-X ligand is shown for each TNP.

To validate the plasmonic response upon sequential ligand exchanges on Au TNPs, it is important to determine that the parent ligands were completely exchanged with different replacement ligands. We performed SERS analysis to quantify the ligands in each exchange step. As displayed in **Figure 7C**, the SERS intensities of the C-S (orange dotted line) and aromatic C=C (blue dotted line) stretches at 1142 and 1605 $cm^{-1}$, respectively, remain

present and constant for each TCA during every step of the exchange reaction (**Figure 7D**). This consistency is expected because exchanging TCA-H by TCA-$N(CH_3)_2$ or TCA-$NO_2$ by TCA-H should not change the overall density of surface passivating ligands, thus the respective SERS intensities of C-S and aromatic C=C stretches should remain same. Furthermore, we observe the disappearance of the N-C stretch at 1372 $cm^{-1}$ (black dotted line) and the appearance of the N-O stretch at 1334 $cm^{-1}$ (green dotted line) when TCA-$N(CH_3)_2$ is replaced on the surface of TNPs by TCA-$NO_2$. Taken together, the structural construct of Au TNP-TCA hybrid conjugates allows reversible manipulation of the interfacial electronic structures thus providing an additional level of tuning the plasmonic properties.

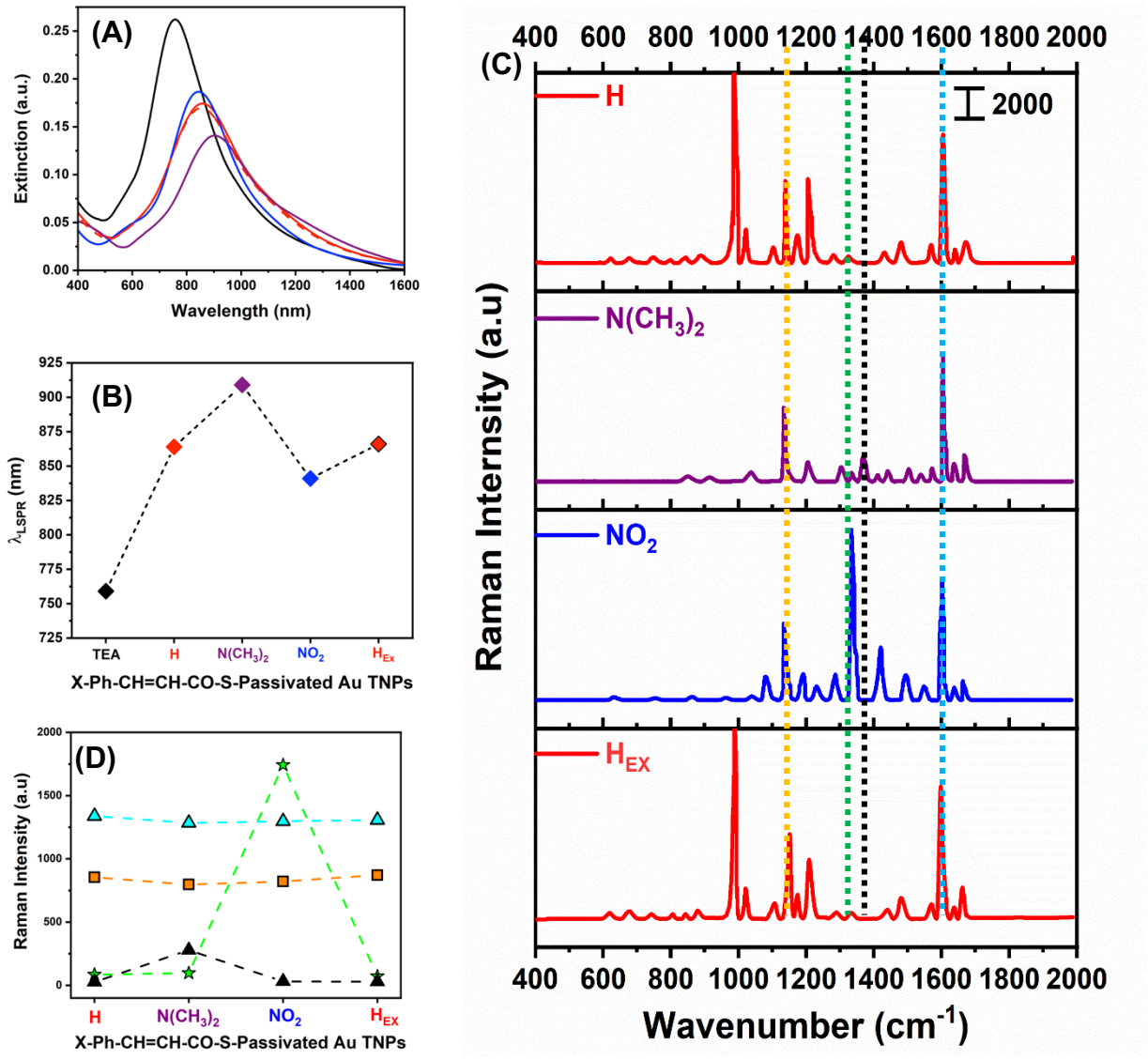


**Figure 7.** **(A)** Experimentally determined LSPR spectra of TEA-passivated Au TNPs (black, 759 nm) and after sequential ligand exchange with TCA-X ligands: -H (red solid), -$N(CH_3)_2$ (purple), -$NO_2$ (blue), and finally back to -H (red dash). $H_{Ex}$ represents final ligand exchange of Au TNPs with TCA-H. **(B)** Values of the LSPR peak position ($\lambda_{LSPR}$) during the sequential ligand exchange of Au TNPs with TCA-X. (C) Experimentally acquired SERS spectra of TCA-X-functionalized Au TNPs during the sequential ligand exchange reactions: -H (red), -$N(CH_3)_2$ (purple), -$NO_2$ (blue), and finally -H ligands

($H_{EX}$, red). Orange, green, black, and blue dotted lines represent the C−S stretch at 1142 $cm^{-1}$, N−O stretch at 1334 $cm^{-1}$, N−C stretch at 1372 $cm^{-1}$, and aromatic C=C stretch at 1605 $cm^{-1}$, respectively. (D) Change in the SERS intensity for different vibrational modes during sequential exchange chemistries: C−S (orange squares), N−O (green stars), N−C (black triangles), aromatic C=C (cyan triangles).

## Concluding Remarks

Through a combination of experimental and theoretical work, we have demonstrated that the interfacial dipole moment at the metal nanostructure-conjugated surface passivating ligand, i.e., hybrid inorganic-organic bonding, plays a crucial role for an extraordinarily larger LSPR peak shift and peak broadening. We have measured the one of the largest known work function changes (~3.3 eV) of Au through the formation of SAMs by exchanging weakly-adsorbed amine ligands with thiolated ligands where stronger Au-ligand interactions create a higher DOS near the $E_F$, allowing facile electron wavefunction delocalization. We have determined an average of ~3.2 electrons/ligand are partially delocalized from Au to the interfacial electronic states. Interestingly, the electronic character (electron donating/withdrawing) of the functional groups does not agree with the trend in the direction of LSPR peak shifts predicted by the Drude model. The plasmon damping of NPs is strongly dependent on the chemical nature of the thiolated ligands in the SAM. Although, we have found that the intrinsic dipole of ligands is a crucial factor in manipulating the Au NP $E_F$ and the thermodynamically-driven interfacial delocalization process, it is alone is not sufficient to explain the observed changes in the plasmonic properties. We have determined that the vinyl conjugation connecting substituted phenyl ring and Au also contributes to the delocalization process. Additionally, we have observed that our chosen ligand system influence the optoelectronic properties (e.g., LSPR wavelength shifts and work function of Au NPs differently that is highly shape dependent. Important, the plasmonic properties of TCA-functionalized Au TNPs are fully reversible upon sequential ligand exchanges replacing parent TCA ligands with incoming ligand having a different substitution. Understanding the origin and effects of SAM-induced dipoles at the interface is critically important in bridging the gap between nanoscopic inorganic-organic hybrid interfacial structures and macroscopic device operation mechanism.

The metal-ligand inorganic-organic hybrid interfacial energy levels play a crucial role in controlling the direct/indirect charge transfer or wavefunction delocalization mechanisms. The present study is fully focused on the delocalization-based mechanism, however, other mechanisms could influence the observed changes in the optoelectronic properties of aromatic ligand-functionalized Au TNPs. Nevertheless, the covalent attachment of TCA ligands to Au is expected to alter the physical and chemical properties of both metal and

ligands, and thus in-depth study and understanding of the physicochemical processes involve at the metal-ligand interface would be highly valuable for construction of future, highly efficient functional plasmonic nanostructures for the fabrication of next generation nanoscale optoelectronic devices[54-58] and the design of highly efficient plasmonic-based photocatalysts.[4, 6, 59]

Tailoring the LSPR response (*i.e.,* LSPR peak shift, width, and intensity) of metal (e.g., Au and Ag) NPs that has traditionally been done through controlling size, shape, and composition, has seen an explosion of effort over the last thirty years.[1, 20, 60] Herein, by deconvoluting the structure-property relationship via ensemble optical measurements along with first principle calculations, we have constructed highly desirable functional plasmonics with a large plasmonic response upon surface modification with our synthesized conjugated aromatic ligands without changing the above-mentioned geometric properties. Although the current study only involves Au TNPs, the knowledge gained can be translated to any shape of Au NPs and other LSPR active metals (e.g., Ag, Cu, Al). Moreover, our quantitative experimental data on manipulating plasmonic responses can be used to benchmark theoretical models of plasmonic properties and predict the effects of electronic and/or chemical structures of surface ligands on LSPR phenomena.

## Experimental Section

**Materials.** Chloro(triethylphosphine) gold (I) ($Et_3PAuCl$, 97%) was purchased from Gelest Inc. Poly(methylhydrosiloxane) (PMHS, $M_n$ = 1700-3300), triethylamine (TEA, 98%), N-(3-Dimethylaminopropyl)-N′-ethylcarbodiimide hydrochloride (EDC, 98%), trans-cinnamic acid (97%), trans-4-(Trifluoromethyl)cinnamic acid (99%), trans-4-Nitrocinnamic acid (97%), trans-4-Methylcinnamic acid (99%), trans-4-Methoxycinnamic acid (99%), trans-4-(Dimethylamino)cinnamic acid (99%), hexadecyltrimethylammonium bromide (CTAB, 98%), gold (III) chloride trihydrate ($HAuCl_4$, 99.9%), sodium borohydride ($NaBH_4$, 99.9%), silver nitrate ($AgNO_3$, 99%), ascorbic acid (AA, 99%), trisodium citrate, and sodium disulfide ($Na_2S$) were purchased from Sigma-Aldrich. ACS grade acetonitrile ($CH_3CN$, 99.9%), ACS grade N, N-Dimethylformamide (DMF, 99.8%), ACS grade Ethyl Acetate (EtOAc, 99.5%), 25 mm x 25 mm glass coverslips, and RBS 35 Detergent were purchased from Fisher Scientific. 3-Mercaptopropyl-trimethoxysilane (MPTMS, 94%) was purchased from Alfa Aesar. Ethanol (200 proof) (EtOH) was purchased from Decon labs. All water was purified using a Thermo Scientific Barnstead Nanopure system.

**Synthesis of Thiocinnamic Acid (TCA) Ligands:** TCA-X ligands were synthesized following a literature published procedure.[61] Briefly, to a DMF solution of cinnamic acid (1.0 mmol) ligands, EDC (1.5 equiv.) was added dropwise at 0 °C under a nitrogen atmosphere. After stirring for 15 mins, finely ground $Na_2S$ (3 equiv.) was added to the reaction mixture which was allowed to stir overnight until the disappearance of the starting material, as confirmed by TLC analysis. The reaction mixture was dissolved in EtOAc (15 mL), and the solution was then carefully acidified to a pH of 2-3 by using 1 M $H_2SO_4$. The organic layer

was then immediately separated and removed under reduced pressure to obtain the crude product. Column purification was performed in silica gel using a 1:9 of acetone:hexane mixture to obtain pure TCA-X ligands.

**Silanization of Glass Coverslips.** 25 x 25 mm dimension glass coverslips were functionalized according to our previously published procedure.[3] Coverslips were sonicated in a 10% (v/v) RBS detergent solution in 90 °C water for 15 min and then rinsed several times with nanopure water, followed by incubation in a 1:1 (v/v) hydrochloric acid: methanol solution for 30 min. Then, coverslips were rinsed several times with nanopure water and were placed in a vacuum oven at 60 °C overnight. The following day, coverslips were brought to room temperature and then incubated in a 15% (v/v) solution of MPTMS in $N_2$ purged ethanolic solution for 30 min. Coverslips were then sonicated in $N_2$ purged ethanol 3x for 15 min each time. After rinsing, coverslips were placed in the vacuum oven at 120 °C for a minimum of 3 hrs. The MPTMS-functionalized coverslips were stored in the vacuum oven up or at 4 °C up to one week for nanoplasmonic sensor fabrication.

**Synthesis of Gold Triangular Nanoprisms (Au TNPs).** Au TNPs were chemically synthesized according to our previously developed procedure with minor modification.[62] Briefly, $Et_3PAu(I)Cl$ (18.0 mg, 0.05 mmol) was dissolved in 40 mL of $N_2$ purged $CH_3CN$ and the solution was stirred for 10 min at room temperature. Stirring was stopped to facilitate the rapid addition of 0.038 mL (0.273 mmol) of TEA into the gold salt solution and then the mixture was heated with resumed stirring. When the temperature of the reaction mixture reached 38°C, 0.6 mL of PMHS was added to form an undisturbed bubble on the side of the reaction flask and then the reaction was allowed to proceed with slow stirring while the temperature was maintained between 38-41°C. During this time, the color of the solution changed from colorless to pink, purple, light blue and then finally a dark navy blue. This dark navy-blue color indicates that the Au TNPs have formed and are approaching the correct edge-length and thickness. At this point, the solution was checked by localized surface plasmon resonance (LSPR) to confirm a stable dipole peak ($\lambda_{LSPR}$) position at 800 nm in $CH_3CN$. If present, the reaction was stopped by removing it from the hot plate followed by centrifugation at 7000 rpm for 10 seconds. Finally, previously prepared MPTMS-functionalized coverslips were incubated in the freshly prepared Au TNPs solution for 1 hr, rinsed with acetonitrile, dried under $N_2$ flow, and then stored under nitrogen at 4°C.

**Synthesis of Gold Nanorods (Au NRs).** Au NRs were synthesized following a literature procedure with modifications.[63] Briefly, a seed solution was prepared at room temperature by mixing 0.25 mL of 10 mM $HAuCl_4$ solution and 7.5 mL 100 mM CTAB solution in a 20 mL vial under vigorous stirring. Next, 0.6 mL of a 10 mM, ice-cold $NaBH_4$ solution was injected into the previously prepared $HAuCl_4$-CTAB solution, which turned yellow from brown, indicating the formation of Au seed. Next, Au NRs were synthesized by adding 0.42 mL of 10 mM $AgNO_3$ and 0.225 mL of 100 mM AA solutions in 37.5 mL 100 mM CTAB solution containing 2 mL of 10 mM $HAuCl_4$. Finally, 48 µL of the as synthesized seed solution was added into the growth solution and left undisturbed at room temperature for 12 hr. Au NRs with ~45 nm of length and 15 nm of diameter were collected via centrifugation for 30 min at 9000 rpm after discarding the supernatant. The aqueous NR solution was kept in a refrigerator at 4 $^{O}$C to crystallize out excess CTAB, which was removed via centrifugation at 4 $^{O}$C. The supernatant containing NRs was used for the incubation of silanized glass coverslips.

**Synthesis of Gold Nanospheres (Au NSs).** Au NSs were synthesized following Frens' method.[64] Briefly, an average 40 nm diameter of gold spherical nanoparticles were prepared by mixing 0.1 mg/ml of $HAuCl_4$ (10-2 % by weight) in 200 ml of nanopure water in a three neck round bottom flask. The solution was brought to boiling, and at this point at 2.0 ml of 10 mg/ml (1% by weight) sodium citrate solution was injected at one-shot. After 5 min, it was a brilliant red color solution. The flask was removed from heat and allowed to cool at room temperature. Analysis of UV-Vis absorption spectra confirmed an LSPR peak around 530 nm indicating formation of 40 nm diameter of Au NSs. The NS solution was stored at 4 $^{O}$C for further use. We used nearly an identical incubation procedure as described for TNPs to attach NSs onto silanized glass substrates.

**TCA functionalization of Au TNPs.** Non-prismatic Au nanostructures from glass coverslip-bound Au TNPs were removed by performing tape-cleaning procedure. An adhesive (Scotch) tape was placed onto the glass substrate, pressed gently with the thumb, and then slowly removed at a 90° angle. The glass coverslip-bound Au TNPs were incubated in 2.0 mM ethanolic solution of TCA ligands overnight. Subsequently, coverslips were rinsed with plenty of ethanol to remove loosely bound TCA ligands, and then the functionalized Au TNPs were dried under $N_2$ flow. We followed the similar experimental procedure for the functionalization of Au NSs and NRs TCA-X ligands.

**Spectroscopy and Microscopy Characterizations.** Absorption and extinction spectra in the range of 400−1600 nm were collected with a Shimadzu UV-3600 Plus UV-VIS-NIR spectrophotometer. All absorption spectra were collected in air with glass coverslips that had been dried under $N_2$ flow. A blank glass coverslip was used as a background. The chemically synthesized Au TNPs attached onto the silanized glass coverslips were characterized using a JEOL 7800F scanning electron microscopy (SEM). Atomic force microscopy (AFM) images were acquired using Bruker Dimension 3000 instrument. The instrument was operated in tapping mode using beam shaped super sharp silicon cantilevers (SSS-NCHR, nanoANDmore) having an average force constant of 42 N/m. The operation frequency of the cantilevers for all measurements was 330 KHz. Surface-enhanced Raman scattering (SERS) analyses were performed on TCA functionalized Au TNP bound glass coverslips using a XploRA Plus Raman microscope from Horiba Scientific. Spectra were obtained using a 785 nm laser excitation source at 100% power, 1800 line/mm grating and 100× objective. An acquisition time of 5 s was used with 5 accumulations from 400-2000 $cm^{-1}$ wavenumber range. All SERS measurements were plotted, and the average Raman intensity was obtained, using Origin software. Ultraviolet photoelectron spectroscopy (UPS) was performed with a Kratos Axis Ultra UPS/XPS spectrometer. UPS spectra were acquired with a 21.2 eV He(I) source at a pass energy of 5.0 eV. A -10 V bias was applied to the sample to increase the kinetic energy of all photoelectrons, improving the instrument response and resolution of the low KE electrons. UPS data were also collected for a piece of Au foil cleaned in the UPS chamber with an $Ar^+$ sputter gun, which allowed measurement of the Fermi level and the work function of gold. No significant photo charging was observed during the UPS analysis of all TCA-functionalized Au TNPs/NRs/NSs samples.

**Theoretical Calculations.** First principles density functional theory (DFT) calculations were performed to determine dipole moment and Raman vibrational frequencies of free ligands and sulfur atom of TCA ligands attached to 3 gold atoms. Time dependent DFT (TDDFT) calculations were used to determine molecular orbital energies of free ligands. Calculations

were carried out for each of the free ligand systems with and without the gold atoms at the BP86 and B3LYP functional levels, respectively, using the Gaussian 16 program.[65] The LANL2DZ basis set was used for the Au atom and the 6−311 + G(d,p) basis set for the other atoms. The optimized structures were visualized using Gaussview.[66] The density of states and molecular orbital energies of the Ligand-Au interface were simulated with ab initio methods by using Vienna ab initio simulation package.[67, 68] The structure was built with Au(100) surface with a 4×4×4 lattice. The ligand was placed on the top surface of the Au slab with a distance of 2 Å. A vacuum slab of 30 Å was added to avoid interaction with the neighbor lattice. The exchange-correlation potential is described as GGA functional Perdew-Burke-Ernzerhof (PBE).[69, 70] For geometry optimization, the top surface of Au and ligand were allowed to relax with the mixture of Davidson and RMM-DIIS algorithms. The electronic convergence is 10-6 eV. The Monkhorst–Pack scheme 2×2×1 k-points mesh was used on Brillouin zone integration. The Gaussian smearing method was used to determine the partial occupancies. The quasi-Newton algorithm is used for ionic relaxation. The DOS calculation uses the tetrahedron method with Blöchl corrections. The dipole correction of direction 3 was enabled to potential. The DOS was analyzed with Vaspkit package,[71] exporting the total density of states and the projected density of each element. The molecular orbital energies of TCA-$Au_3$ systems were obtained by optimizing the geometry and running charge density calculation self-consistently. Vaspkit package was used to generate a K-path based on the charge density results and a non-self-consistent charge density calculation at desired K points was performed. The charge density with the eigenvalues were the post-processed by Vaspkit to generate the molecular orbital energies and the band gap.

**Finite Domain Time Difference (FDTD) Calculations.** Electromagnetic field simulation and simulation extracting extinction spectra of Nanoprism were performed by using a commercial-grade FDTD simulator from Lumerical Solutions, Inc. As depicted in **Figure 1C**, the size of triangular prism was at 42 nm of edge length and 9 nm of height, whereas the diameter of the Au NS is fixed 40 nm, and the length and diameter of au NRs are 40 and 15 nm, respectively.The dielectric constant of the prism material was obtained from Johnson and Christy model of gold as available in the software. Light in the form of total-field scattered-field is propagating along with polarization parallel to the edge length of the prism in the XY plane. This light source was positioned at 35 nm apart from the prism, with a total dimesnion of 70 nm both in X and Y directions. We follow the same procedure for NSs and NRs. Scattered light was collected by a monitor in XY-plane with a total dimension of 60 nm spanned both in X axis and Y axis. The perfectly matched layer (PML) was applied at the boundary condition. Simulation volume was 80 nm in X, Y and Z directions with maximum mesh step settings as 0.5 nm in all directions and was assumed to be filled with air, having refractive index of 1.0.

**Acknowledgements**

This work was primarily supported by research funding provided by NSF grant (CBET-1604617 and 2204681). We thank Dr. C. Donley at UNC-Chapel hill for assisting with the UPS analysis. Authors also thank M. Vitoria Simas for helping with the Au NR synthesis.

**Author contributions**

R.S. and S.H. conceived the original idea, designed the research plan. S.H. synthesized and characterized all the TCA-X ligands, performed all the LSPR- and Raman-related experiments, and conducting LSPR, Raman, and UPS data analysis. X.Y., Z.P., and J.Z. performed DFT calculations. P.G. conducted the AFM analysis. S.H., B.B.M., and R.S. co-wrote the manuscript, and other authors contributed to reviewing and editing the manuscript.

**Supporting Information.** The supporting Information is available free of charge at https://pubs.acs.org. Description for dipole moment and free carrier density calculations, characterization data for TCA-X ligands, additional UV-Vis extinction of various organothiolate ligand-functionalized Au TNPs, Raman spectra and UPS spectra, energy level diagram, SEM and AFM images of Au TNPs, and tables.

## Conflict of Interest

The authors declare no conflict of interest.

**References:**


(1) Mayer, K. M.; Hafner, J. H. Localized surface plasmon resonance sensors. *Chemical Reviews* **2011**, *111* (6), 3828-3857.
(2) Anker, J. N.; Hall, W. P.; Lyandres, O.; Shah, N. C.; Zhao, J.; Van Duyne, R. P. Biosensing with plasmonic nanosensors. *Nature Materials* **2008**, *7* (6), 442-453.
(3) Joshi, G. K.; Deitz-McElyea, S.; Liyanage, T.; Lawrence, K.; Mali, S.; Sardar, R.; Korc, M. Label-free nanoplasmonic-based short noncoding RNA sensing at attomolar concentrations allows for quantitative and highly specific assay of microRNA-10b in biological fluids and circulating exosomes. *ACS Nano* **2015**, *9* (11), 11075-11089.
(4) Aslam, U.; Rao, V. G.; Chavez, S.; Linic, S. Catalytic conversion of solar to chemical energy on plasmonic metal nanostructures. *Nature Catalysis* **2018**, *1* (9), 656-665.
(5) Zhang, Y.; He, S.; Guo, W.; Hu, Y.; Huang, J.; Mulcahy, J. R.; Wei, W. D. Surface-plasmon-driven hot electron photochemistry. *Chemical reviews* **2017**, *118* (6), 2927-2954.
(6) Zhou, L.; Swearer, D. F.; Zhang, C.; Robatjazi, H.; Zhao, H.; Henderson, L.; Dong, L.; Christopher, P.; Carter, E. A.; Nordlander, P.; et al. Quantifying hot carrier and thermal contributions in plasmonic photocatalysis. *Science* **2018**, *362* (6410), 69-72.
(7) Knight, M. W.; Sobhani, H.; Nordlander, P.; Halas, N. J. Photodetection with active optical antennas. *Science* **2011**, *332* (6030), 702-704.
(8) Atwater, H. A.; Polman, A. Plasmonics for improved photovoltaic devices. *Nature Materials* **2010**, *9* (3), 205-213.
(9) Kinkhabwala, A.; Yu, Z.; Fan, S.; Avlasevich, Y.; Müllen, K.; Moerner, W. Large single-molecule fluorescence enhancements produced by a bowtie nanoantenna. *Nature photonics* **2009**, *3* (11), 654-657.
(10) Curto, A. G.; Volpe, G.; Taminiau, T. H.; Kreuzer, M. P.; Quidant, R.; Van Hulst, N. F. Unidirectional emission of a quantum dot coupled to a nanoantenna. *Science* **2010**, *329* (5994), 930-933.
(11) Zijlstra, P.; Paulo, P. M.; Orrit, M. Optical detection of single non-absorbing molecules using the surface plasmon resonance of a gold nanorod. *Nature nanotechnology* **2012**, *7* (6), 379-382.
(12) Lee, S. A.; Link, S. Chemical Interface Damping of Surface Plasmon Resonances. *Accounts of Chemical Research* **2021**, *54* (8), 1950-1960.
(13) Liyanage, T.; Nagaraju, M.; Johnson, M.; Muhoberac, B. B.; Sardar, R. Reversible tuning of the plasmoelectric effect in noble metal nanostructures through manipulation of organic ligand energy levels. *Nano Letters* **2019**, *20* (1), 192-200.
(14) Foerster, B.; Joplin, A.; Kaefer, K.; Celiksoy, S.; Link, S.; Sönnichsen, C. Chemical interface damping depends on electrons reaching the surface. *ACS Nano* **2017**, *11* (3), 2886-2893.
(15) Foerster, B.; Spata, V. A.; Carter, E. A.; Sönnichsen, C.; Link, S. Plasmon damping depends on the chemical nature of the nanoparticle interface. *Science Advances* **2019**, *5* (3), eaav0704.
(16) Lee, S. Y.; Tsalu, P. V.; Kim, G. W.; Seo, M. J.; Hong, J. W.; Ha, J. W. Tuning chemical interface damping: interfacial electronic effects of adsorbate molecules and sharp tips of single gold bipyramids. *Nano Letters* **2019**, *19* (4), 2568-2574.
(17) Alloway, D. M.; Graham, A. L.; Yang, X.; Mudalige, A.; Colorado Jr, R.; Wysocki, V. H.; Pemberton, J. E.; Lee, T. R.; Wysocki, R. J.; Armstrong, N. R. Tuning the effective work function of gold and silver using ω-functionalized alkanethiols: varying surface composition through dilution and choice of terminal groups. *The Journal of Physical Chemistry C* **2009**, *113* (47), 20328-20334.
(18) Rusu, P. C.; Brocks, G. Surface dipoles and work functions of alkylthiolates and fluorinated alkylthiolates on Au (111). *The Journal of Physical Chemistry B* **2006**, *110* (45), 22628-22634.

(19) Ford, W. E.; Gao, D.; Knorr, N.; Wirtz, R.; Scholz, F.; Karipidou, Z.; Ogasawara, K.; Rosselli, S.; Rodin, V.; Nelles, G. Organic dipole layers for ultralow work function electrodes. *ACS nano* **2014**, *8* (9), 9173-9180.
(20) Halas, N. J.; Lal, S.; Chang, W.-S.; Link, S.; Nordlander, P. Plasmons in strongly coupled metallic nanostructures. *Chemical Reviews* **2011**, *111* (6), 3913-3961.
(21) Duan, H.; Fernández-Domínguez, A. I.; Bosman, M.; Maier, S. A.; Yang, J. K. Nanoplasmonics: classical down to the nanometer scale. *Nano letters* **2012**, *12* (3), 1683-1689.
(22) Koh, A. L.; Fernández-Domínguez, A. I.; McComb, D. W.; Maier, S. A.; Yang, J. K. High-resolution mapping of electron-beam-excited plasmon modes in lithographically defined gold nanostructures. *Nano letters* **2011**, *11* (3), 1323-1330.
(23) Mulvaney, P. Surface plasmon spectroscopy of nanosized metal particles. *Langmuir* **1996**, *12* (3), 788-800.
(24) Goldmann, C.; Lazzari, R.; Paquez, X.; Boissière, C.; Ribot, F.; Sanchez, C.; Chanéac, C.; Portehault, D. Charge transfer at hybrid interfaces: plasmonics of aromatic thiol-capped gold nanoparticles. *ACS nano* **2015**, *9* (7), 7572-7582.
(25) Thomas, R.; Thomas, A.; Pullanchery, S.; Joseph, L.; Somasundaran, S. M.; Swathi, R. S.; Gray, S. K.; Thomas, K. G. Plexcitons: the role of oscillator strengths and spectral widths in determining strong coupling. *ACS nano* **2018**, *12* (1), 402-415.
(26) Novo, C.; Gomez, D.; Perez-Juste, J.; Zhang, Z.; Petrova, H.; Reismann, M.; Mulvaney, P.; Hartland, G. V. Contributions from radiation damping and surface scattering to the linewidth of the longitudinal plasmon band of gold nanorods: a single particle study. *Physical Chemistry Chemical Physics* **2006**, *8* (30), 3540-3546.
(27) Sönnichsen, C.; Franzl, T.; Wilk, T.; von Plessen, G.; Feldmann, J.; Wilson, O.; Mulvaney, P. Drastic reduction of plasmon damping in gold nanorods. *Physical review letters* **2002**, *88* (7), 077402.
(28) Joshi, G. K.; Blodgett, K. N.; Muhoberac, B. B.; Johnson, M. A.; Smith, K. A.; Sardar, R. Ultrasensitive photoreversible molecular sensors of azobenzene-functionalized plasmonic nanoantennas. *Nano Letters* **2014**, *14* (2), 532-540.
(29) Masterson, A. N.; Hati, S.; Ren, G.; Liyanage, T.; Manicke, N. E.; Goodpaster, J. V.; Sardar, R. Enhancing nonfouling and sensitivity of surface-enhanced Raman scattering substrates for potent drug analysis in blood plasma via fabrication of a flexible plasmonic patch. *Analytical Chemistry* **2021**, *93* (4), 2578-2588.
(30) Crivillers, N.; Osella, S.; Van Dyck, C.; Lazzerini, G. M.; Cornil, D.; Liscio, A.; Di Stasio, F.; Mian, S.; Fenwick, O.; Reinders, F. Large work function shift of gold induced by a novel perfluorinated azobenzene-based self-assembled monolayer. *Advanced materials* **2013**, *25* (3), 432-436.
(31) Heimel, G.; Romaner, L.; Brédas, J.-L.; Zojer, E. Interface energetics and level alignment at covalent metal-molecule junctions: π-conjugated thiols on gold. *Physical Review Letters* **2006**, *96* (19), 196806.
(32) Narasimha, K. T.; Ge, C.; Fabbri, J. D.; Clay, W.; Tkachenko, B. A.; Fokin, A. A.; Schreiner, P. R.; Dahl, J. E.; Carlson, R. M.; Shen, Z. X.; et al. Ultralow effective work function surfaces using diamondoid monolayers. *Nat Nanotechnol* **2016**, *11* (3), 267-272. From NLM PubMed-not-MEDLINE.
(33) LaRue, J. L.; White, J. D.; Nahler, N. H.; Liu, Z.; Sun, Y.; Pianetta, P. A.; Auerbach, D. J.; Wodtke, A. M. The work function of submonolayer cesium-covered gold: a photoelectron spectroscopy study. *J Chem Phys* **2008**, *129* (2), 024709. From NLM PubMed-not-MEDLINE.
(34) Saito, N.; Ryuzaki, S.; Tsuji, Y.; Noguchi, Y.; Matsuda, R.; Wang, P.; Tanaka, D.; Arima, Y.; Okamoto, K.; Yoshizawa, K. Effect of chemically induced permittivity changes on the plasmonic properties of metal nanoparticles. *Communications Materials* **2021**, *2* (1), 1-8.
(35) Romaner, L.; Heimel, G.; Brédas, J.-L.; Gerlach, A.; Schreiber, F.; Johnson, R. L.; Zegenhagen, J.; Duhm, S.; Koch, N.; Zojer, E. Impact of bidirectional charge transfer and molecular distortions on the electronic structure of a metal-organic interface. *Physical review letters* **2007**, *99* (25), 256801.

(36) Natan, A.; Zidon, Y.; Shapira, Y.; Kronik, L. Cooperative effects and dipole formation at semiconductor and self-assembled-monolayer interfaces. *Physical Review B* **2006**, *73* (19), 193310.
(37) Sushko, M. L.; Shluger, A. L. Intramolecular Dipole Coupling and Depolarization in Self-Assembled Monolayers. *Advanced Functional Materials* **2008**, *18* (15), 2228-2236.
(38) Jackson, J. *Classical Electrodynamics* Willey, New York, 1975.
(39) Neuman, O.; Naaman, R. New optical absorption band resulting from the organization of self-assembled monolayers of organic thiols on gold. *The Journal of Physical Chemistry B* **2006**, *110* (11), 5163-5165.
(40) Ray, S.; Cohen, H.; Naaman, R.; Liu, H.; Waldeck, D. Organization-induced charge redistribution in self-assembled organic monolayers on gold. *The Journal of Physical Chemistry B* **2005**, *109* (29), 14064-14073.
(41) Hartland, G. V.; Besteiro, L. V.; Johns, P.; Govorov, A. O. What's so hot about electrons in metal nanoparticles? *ACS Energy Letters* **2017**, *2* (7), 1641-1653.
(42) Wu, K.; Chen, J.; Mcbride, J. R.; Lian, T. Efficient hot-electron transfer by a plasmon-induced interfacial charge-transfer transition. *Science* **2015**, *349* (6248), 632-635.
(43) Prusty, G.; Lee, J. T.; Seifert, S.; Muhoberac, B. B.; Sardar, R. Ultrathin plasmonic tungsten oxide quantum wells with controllable free carrier densities. *Journal of the American Chemical Society* **2020**, *142* (13), 5938-5942.
(44) Luther, J. M.; Jain, P. K.; Ewers, T.; Alivisatos, A. P. Localized surface plasmon resonances arising from free carriers in doped quantum dots. *Nat Mater* **2011**, *10* (5), 361-366. From NLM PubMed-not-MEDLINE.
(45) Govorov, A. O.; Zhang, H.; Gun'ko, Y. K. Theory of Photoinjection of Hot Plasmonic Carriers from Metal Nanostructures into Semiconductors and Surface Molecules. *The Journal of Physical Chemistry C* **2013**, *117* (32), 16616-16631.
(46) Jung, I.; Kim, M.; Kwak, M.; Kim, G.; Jang, M.; Kim, S. M.; Park, D. J.; Park, S. Surface plasmon resonance extension through two-block metal-conducting polymer nanorods. *Nature Communications* **2018**, *9* (1), 1-9.
(47) Liao, P. F.; Wokaun, A. Lightning rod effect in surface enhanced Raman scattering. *The Journal of Chemical Physics* **1982**, *76*, 751-752.
(48) Zijlstra, P.; Paulo, P. M.; Yu, K.; Xu, Q. H.; Orrit, M. Chemical interface damping in single gold nanorods and its near elimination by tip-specific functionalization. *Angew Chem Int Ed Engl* **2012**, *51* (33), 8352-8355. From NLM PubMed-not-MEDLINE.
(49) Alloway, D. M.; Hofmann, M.; Smith, D. L.; Gruhn, N. E.; Graham, A. L.; Colorado Jr, R.; Wysocki, V. H.; Lee, T. R.; Lee, P. A.; Armstrong, N. R. Interface Dipoles Arising from Self-Assembled Monolayers on Gold: UV− Photoemission Studies of Alkanethiols and Partially Fluorinated Alkanethiols. *The Journal of Physical Chemistry B* **2003**, *107* (42), 11690-11699.
(50) Kim, J.-Y.; Han, M.-G.; Lien, M.-B.; Magonov, S.; Zhu, Y.; George, H.; Norris, T. B.; Kotov, N. A. Dipole-like electrostatic asymmetry of gold nanorods. *Science Advances* **2018**, *4* (2), e1700682.
(51) Janicek, B. E.; Hinman, J. G.; Hinman, J. J.; Bae, S. H.; Wu, M.; Turner, J.; Chang, H.-H.; Park, E.; Lawless, R.; Suslick, K. S. Quantitative imaging of organic ligand density on anisotropic inorganic nanocrystals. *Nano letters* **2019**, *19* (9), 6308-6314.
(52) Shibu Joseph, S.; Ipe, B. I.; Pramod, P.; Thomas, K. G. Gold nanorods to nanochains: mechanistic investigations on their longitudinal assembly using α, ω-alkanedithiols and interplasmon coupling. *The Journal of Physical Chemistry B* **2006**, *110* (1), 150-157.
(53) Sheldon, M. T.; Van de Groep, J.; Brown, A. M.; Polman, A.; Atwater, H. A. Plasmoelectric potentials in metal nanostructures. *Science* **2014**, *346* (6211), 828-831.
(54) Seker, F.; Malenfant, P. R.; Larsen, M.; Alizadeh, A.; Conway, K.; Kulkarni, A. M.; Goddard, G.; Garaas, R. On-Demand Control of Optoelectronic Coupling in Gold Nanoparticle Arrays. *Advanced Materials* **2005**, *17* (16), 1941-1945.
(55) Ravi, S. K.; Sun, W.; Nandakumar, D. K.; Zhang, Y.; Tan, S. C. Optical manipulation of work function contrasts on metal thin films. *Science advances* **2018**, *4* (3), eaao6050.

(56) Gravelsins, S.; Park, M. J.; Niewczas, M.; Hyeong, S.-K.; Lee, S.-K.; Ahmed, A.; Dhirani, A.-A. Large emergent optoelectronic enhancement in molecularly cross-linked gold nanoparticle nanosheets. *Communications Chemistry* **2022**, *5* (1), 103.
(57) Lee, H.; Kim, M.; Kim, I.; Lee, H. Flexible and stretchable optoelectronic devices using silver nanowires and graphene. *Advanced Materials* **2016**, *28* (22), 4541-4548.
(58) Heo, M.; Cho, H.; Jung, J. W.; Jeong, J. R.; Park, S.; Kim, J. Y. High-performance organic optoelectronic devices enhanced by surface plasmon resonance. *Advanced Materials* **2011**, *23* (47), 5689-5693.
(59) Linic, S.; Aslam, U.; Boerigter, C.; Morabito, M. Photochemical transformations on plasmonic metal nanoparticles. *Nature Materials* **2015**, *14* (6), 567-576.
(60) Rycenga, M.; Cobley, C. M.; Zeng, J.; Li, W.; Moran, C. H.; Zhang, Q.; Qin, D.; Xia, Y. Controlling the synthesis and assembly of silver nanostructures for plasmonic applications. *Chemical reviews* **2011**, *111* (6), 3669-3712.
(61) Vishwanatha, T.; Samarasimhareddy, M.; Sureshbabu, V. V. Facile N-Urethane-Protected α-Amino/Peptide Thioacid Preparation Using EDC and Na2S. *Synlett* **2012**, *2012* (01), 89-92.
(62) Joshi, G. K.; McClory, P. J.; Muhoberac, B. B.; Kumbhar, A.; Smith, K. A.; Sardar, R. Designing efficient localized surface plasmon resonance-based sensing platforms: Optimization of sensor response by controlling the edge length of gold nanoprisms. *The Journal of Physical Chemistry C* **2012**, *116* (39), 20990-21000.
(63) Gole, A.; Murphy, C. J. Azide-derivatized gold nanorods: functional materials for “click” chemistry. *Langmuir* **2008**, *24* (1), 266-272.
(64) Frens, G. Controlled nucleation for the regulation of the particle size in monodisperse gold suspensions. *Nature physical science* **1973**, *241* (105), 20-22.
(65) Frisch, M.; Trucks, G.; Schlegel, H.; Scuseria, G.; Robb, M.; Cheeseman, J.; Scalmani, G.; Barone, V.; Petersson, G.; Nakatsuji, H. Gaussian 16, Revision A. 03, Gaussian. *Inc., Wallingford CT* **2016**, *3*.
(66) Dennington, R.; Keith, T. A.; Millam, J. M. GaussView 6.0. 16. *Semichem Inc.: Shawnee Mission, KS, USA* **2016**.
(67) Kresse, G.; Furthmüller, J. Efficient iterative schemes for ab initio total-energy calculations using a plane-wave basis set. *Physical review B* **1996**, *54* (16), 11169.
(68) Kresse, G.; Furthmüller, J. Efficiency of ab-initio total energy calculations for metals and semiconductors using a plane-wave basis set. *Computational materials science* **1996**, *6* (1), 15-50.
(69) Perdew, J. P.; Burke, K.; Ernzerhof, M. Generalized gradient approximation made simple. *Physical review letters* **1996**, *77* (18), 3865-3868.
(70) Perdew, J. P.; Burke, K.; Ernzerhof, M. Generalized Gradient Approximation Made Simple *Physical Review Letters* **1997**, *78* (7), 1396-1396.
(71) Wang, V.; Xu, N.; Liu, J.-C.; Tang, G.; Geng, W.-T. VASPKIT: A user-friendly interface facilitating high-throughput computing and analysis using VASP code. *Computer Physics Communications* **2021**, *267*, 108033.